

# Thermal Hall Effect and Neutral Spinons in a Doped Mott Insulator

Zhi-Jian Song,<sup>1</sup> Jia-Xin Zhang,<sup>1,\*</sup> and Zheng-Yu Weng<sup>1</sup>

<sup>1</sup>*Institute for Advanced Study, Tsinghua University, Beijing 100084, China*

(Dated: September 13, 2023)

In the pseudogap phase of the cuprate, a thermal Hall response of neutral objects has been recently detected experimentally, which continuously persists into the antiferromagnetic insulating phase. In this work, we study the transport properties of neutral spinons as the elementary excitation of a doped Mott insulator, which is governed by a mutual Chern-Simons topological gauge structure. We show that such a chiral spinon as a composite of an  $S = 1/2$  spin sitting at the core of a supercurrent vortex, can contribute to the thermal Hall effect, thermopower, and Hall effect due to its intrinsic transverse (cyclotron) motion under internal fictitious fluxes. In particular, the magnitudes of the transport coefficients are phenomenologically determined by two basic parameters: the doping concentration and  $T_c$ , quantitatively consistent with the experimental measurements including the signs and qualitative temperature and magnetic field dependence. Combined with the predictions of the spinon longitudinal transport properties, including the Nernst and spin Hall effects, a phenomenological description of the pseudogap phase is established as characterized by the neutral spinon excitations, which eventually become “confined” with an intrinsic superconducting transition at  $T_c$ . Finally, within this theoretical framework, the “order to order” phase transition between the superconducting and antiferromagnetic insulating phases are briefly discussed, with the thermal Hall monotonically increasing into the latter.

## I. INTRODUCTION

Transport measurements serve as a powerful tool to gain insight into the nature of elementary excitations in the cuprates [1, 2]. The anomalous signals detected in these measurements are crucial for a systematic understanding at the microscopic level. For instance, the Hall number in the cuprates indicates a discontinuity at a doping  $p^*$ , which corresponds to the doping concentration at which the pseudogap (PG) phase terminates [3, 4]. Within the PG phase, when  $p < p^*$ , the Hall number aligns with the doping density  $p$ , which seemingly contrasts with free systems where the large Fermi surface encloses an area of  $1 + p$  as indicated experimentally at  $p > p^*$ . Previous studies have hypothesized that this discrepancy might stem from Fermi surface reconstruction due to antiferromagnetic (AFM) order with  $Q = (\pi, \pi)$  [5] or in the absence of the explicit translation symmetry breaking due to strong correlations [6, 7].

Furthermore, a linear magnetic-field dependent thermal Hall signal [8–10] in the family of the cuprate compounds has been recently observed at  $p < p^*$ , extending to the AFM insulating phase. It is important to underscore that the experimental signal exhibits no effect for the magnetic field that is aligned parallel to the copper-oxide plane [9], which implies that the thermal Hall effect is originated from an orbit effect. Prior theoretical studies [11, 12] suggest that in the case of the cuprates, magnons on a square lattice will fail to yield a nonzero thermal Hall conductivity when subjected to either the Dzyaloshinskii-Moriya spin interaction or the localized formation of skyrmion defects. Additionally,

the phenomenological descriptions involve neutral excitations like spinons [12–14] and phonons [15–17] have been proposed. Phenomenologically a universal behavior with a scaling law was proposed [18]. Besides the cuprates, the sizeable thermal Hall effect has been also found in spin-ice  $\text{Tb}_2\text{Ti}_2\text{O}_7$  [19] and spin liquid  $\text{RuCl}_3$  [20] as well as the Kitaev materials [21]. Moreover, both integer [22, 23] and fractional [24] quantum Hall systems (QHE & FQHE) offer a unique perspective, where the thermal Hall effect finds its explanation in the conformal field theory (CFT) of chiral edge modes [25].

The transport measurements provide a direct probe into the contribution of the excitations that dominate the PG phase. The neutral spinon in the PG phase is an essential elementary excitation in the strongly correlated theories of doped Mott insulators. Thus, if and how the neutral spinon participates in the thermal Hall and other transport phenomena become important issues that should be addressed very seriously. In this paper, we shall make a self-consistent study of spinon transport within the framework of the phase-string theory [26, 27]. The spinon predicted in this theory is different from either the slave-boson or slave-fermion approaches [1, 28–31] due to the so-called phase-string effect [32–34] hidden in the  $t$ - $J$  model upon doping, which is a topological Berry phase replacing the usual Fermi sign structure in the restricted Hilbert space. Specifically:

1. Each spinon undergoes a cyclotron motion due to an intrinsic Berry curvature caused by the phase-string effect [cf. Fig. 1(a)]. The time-reversal symmetry is retained in the absence of external magnetic fields as the opposite spins see the opposite fictitious fluxes with the opposite chiral edge currents [cf. Fig. 1(b-c)]. The system is distinct from the usual topological insulator [35, 36] in that all the spinons with opposite chiralities are RVB-paired in

\* zjx19@mails.tsinghua.edu.cn

the ground state.

- Each spinon is always locked with a charge-current vortex. Since an external perpendicular magnetic field must be balanced by the net (polarized) vortices, then unpaired (free) *chiral* spinons must be generated from the RVB condensate, which contributes to the novel transport in the PG phase.
- The cyclotron motion of the spinon and its locking with the charge vortex [cf. Fig. 1(a)] are mathematically characterized by a mutual Chern-Simons gauge structure, which will contribute to unconventional transport phenomena, including the thermopower effect [cf. Fig. 1(d)], thermal Hall [cf. Fig. 1(e)], and Hall effect [cf. Fig. 1(f)].

We shall investigate the above spinon transport by using a semiclassical approach based on the mutual Chern-Simons gauge theory. The calculated results are essentially determined by the basic parameters of doping concentration as well as  $T_c$ , with the magnitudes comparable with the experimental measurements [3, 4, 8–10, 37, 38]. Also more physical implications arising from such neutral spinons as the elementary excitations will be briefly discussed in Sec. IV D, which can explain the Nernst effect [39–41] and the scaling relationship between  $T_c$  and the spin resonance energy as observed in neutron measurements [42–45]. Especially an “order-to-order” phase transition between the superconducting and AFM insulating phases can also naturally emerge within the same theoretical framework.

## II. MUTUAL CHERN-SIMONS GAUGE THEORY OF THE DOPED MOTT INSULATOR

### A. Topological Gauge Structure

Phase-string theory of the doped Mott insulator is based on a nontrivial sign structure identified in both the  $t$ - $J$  model [32–34] and the Hubbard model [46, 47], in which the conventional Fermi statistics of the electrons are replaced by the phase-string sign structure in the restricted Hilbert space of the lower (upper) Hubbard band. In the phase-string theory, such a sign structure is further precisely mapped to a topological gauge structure. The corresponding low-energy description involves the mutual Chern-Simons (MCS) gauge interaction between the spin and charge degrees of freedom [48–52], governed by the lattice Euclidean Lagrangian

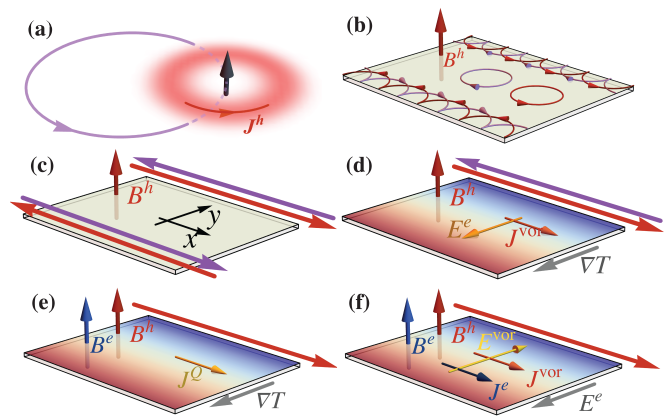


FIG. 1. (a) A schematic illustration of a chiral spinon with a mutual Chern-Simons gauge structure: a neutral  $S = 1/2$  spin (black arrow) sitting at the core of an induced supercurrent vortex (red ring), which itself sees an intrinsic magnetic field  $B^h$  to undergo a cyclotron motion (purple circle) self-consistently; (b) The semi-classical behavior of the chiral spinons under a uniform  $B^h$  in the bulk and edges of the sample, and (c) the resultant vortex edge currents with opposite chiralities. Note that in the equilibrium state no time-reversal symmetry is broken as the opposite spins see the opposite sign of  $B^h$  with the compensation of the opposite cyclotron motion and edge currents (red and purple with arrows); (d) Temperature gradient  $\nabla T$  breaks the equilibrium between the opposite edges, causing net vortex current  $\mathbf{J}^{\text{vor}}$  and electric field in the sample, which contributes to a thermopower effect; (e) External perpendicular magnetic field  $B^e$  (blue arrow) and the in-plane temperature gradient  $\nabla T$  break the balance of the chirality of spinon-vortices to generate a net thermal current  $\mathbf{J}^Q$ , which contributes to a thermal Hall effect; (f) An applied charge current  $\mathbf{J}^e$  induces a force  $\mathbf{E}^{\text{vor}}$  on the spinon-vortex, which generates a vortex current  $\mathbf{J}^{\text{vor}}$  in the presence of an external magnetic field  $B^e$  to produce a net electric field  $E^e$ . The resulting Hall effect gives rise to the Hall number precisely equal to the doping concentration  $\delta$  at low temperature.

$L = L_h + L_s + L_{\text{MCS}}$  as follows:

$$L_h = \sum_I h_I^\dagger [\partial_\tau - iA_0^s(I) - iA_0^e(I) + \mu_h] h_I - t_h \sum_{i\alpha} \left[ h_I^\dagger h_{I+\alpha} e^{i\mathbf{A}_\alpha^s(I) + i\mathbf{A}_\alpha^e(I)} + \text{h.c.} \right], \quad (1)$$

$$L_s = \sum_{i\sigma} b_{i\sigma}^\dagger \left[ \partial_\tau - i\sigma A_0^h(i) + \lambda_b + \frac{1}{2}g\mu_B B^e \sigma \right] b_{i\sigma} - J_s \sum_{i\alpha\sigma} \left[ b_{i\sigma}^\dagger b_{i+\alpha, \bar{\sigma}}^\dagger e^{i\sigma \mathbf{A}_\alpha^h(i)} + \text{h.c.} \right], \quad (2)$$

$$L_{\text{MCS}} = \frac{i}{\pi} \sum_i \epsilon^{\mu\nu\lambda} A_\mu^s(I) \partial_\nu A_\lambda^h(i), \quad (3)$$

in which  $L_h$  and  $L_s$  describe the dynamics of the matter fields—bosonic spinless holon  $h_I$ , and bosonic neutral spinon  $b_{i\sigma}$  (with  $\bar{\sigma} \equiv -\sigma$ ), respectively. The indices  $\alpha$  and  $\beta$  denote only the spatial components:  $x, y$ , and the indices  $\mu = (\tau, \mathbf{r})$  label the full time-space vector, with

the indices  $i, I$  representing the two-dimensional (2D) square lattice site and its dual lattice site, respectively. The external magnetic vector potential  $\mathbf{A}^e$  with the field strength  $B^e$  perpendicular to the 2D plane, interacts with the charge (holon) degree of freedom through the orbit effect (setting the charge equal to one) in Eq. (1), and the spin degree of freedom via a Zeeman effect in Eq. (2).

Here the holon field  $h$  and spinon field  $b$  minimally couple to the gauge fields,  $A_\mu^s$  and  $A_\mu^h$ , respectively, with the MCS topological structure given in Eq. (3). It implies that the holon (spinon) number  $n_I^h$  ( $n_i^b$ ) will determine the gauge-field strength of  $A_\mu^h$  ( $A_\mu^s$ ) as if each matter particle (holon or spinon) is attached to a fictitious  $\pi$  flux tube visible only by a different species. This can be directly seen by considering the following equations of motion for  $A_0^s$  and  $A_0^h$ , respectively:

$$\frac{\partial L}{\partial A_0^s(I)} = 0 \Rightarrow \pi n_I^h = \epsilon^{\alpha\beta} \partial_\alpha \mathbf{A}_\beta^h(i) \equiv B^h, \quad (4)$$

$$\frac{\partial L}{\partial A_0^h(i)} = 0 \Rightarrow \pi \sum_\sigma \sigma n_{i\sigma}^b = \epsilon^{\alpha\beta} \partial_\alpha \mathbf{A}_\beta^s(I) \equiv B^s. \quad (5)$$

Similarly, by using the charge (holon) current  $\mathbf{J}_\alpha^h(I) \equiv \partial L_h / \partial \mathbf{A}_\alpha^s(I)$  and spin current associated with the  $b$ -spinon:  $\mathbf{J}_\alpha^{\text{spin}}(i) \equiv \partial L_s / \partial \mathbf{A}_\alpha^h(i)$ , one has the following equations of motion for  $\mathbf{A}_\alpha^s(I)$  and  $\mathbf{A}_\alpha^h(i)$ , respectively:

$$\frac{\partial L}{\partial \mathbf{A}_\alpha^h(i)} = 0 \Rightarrow \pi \mathbf{J}_\alpha^{\text{spin}}(i) = \epsilon_{\alpha\beta} \mathbf{E}_\beta^s(i), \quad (6)$$

$$\frac{\partial L}{\partial \mathbf{A}_\alpha^s(I)} = 0 \Rightarrow \pi \mathbf{J}_\alpha^h(I) = \epsilon_{\alpha\beta} \mathbf{E}_\beta^h(I), \quad (7)$$

where  $\mathbf{E}_\alpha^{s/h} = \partial_0 \mathbf{A}_\alpha^{s/h} - \partial_\alpha A_0^{s/h}$ . Therefore, due to the  $U(1) \times U(1)$  mutual Chern-Simons gauge structure, the conserved charge (holon) and spin density-currents are constrained to the internal gauge field strengths by the equations of motion in Eqs.(4)-(7).

## B. Low-temperature Pseudogap phase.

At half-filling with  $n_I^h = 0$ , one has  $\mathbf{A}_\beta^h(i) = 0$ , and  $L \rightarrow L_s$  reduces to the Schwinger-boson mean-field state Lagrangian that well describes the AFM phase. On the other hand, at finite doping, the Bose condensation of the bosonic holon field will define a low-temperature PG phase [49, 50]. As the holons are condensed, the total gauge fluctuations in  $L_h$  of Eq.(1) will be suppressed due to the Higgs mechanism, leading to

$$\mathbf{A}_\alpha^s(I) + \mathbf{A}_\alpha^e(I) - 2\pi m_\alpha(I) = 0, \quad (8)$$

where  $m_\alpha \in \mathbb{Z}$  comes from the compactness of the spatial components in Eq. (1). By using Eq. (8), the equations of motion Eq. (5) and Eq. (6) can be reformulated as:

$$\pi \sum_\sigma \sigma n_{i\sigma}^b - 2\pi J_0^{2\pi}(i) + \Phi^e(i) = 0, \quad (9)$$

$$\pi \mathbf{J}_\alpha^{\text{spin}}(i) - 2\pi \mathbf{J}_\alpha^{2\pi}(i) + \epsilon_{\alpha\beta} \mathbf{E}_\beta^e(i) = 0, \quad (10)$$

where  $\Phi^e = \epsilon_{\alpha\beta} \Delta_\alpha \mathbf{A}_\beta^e$  and  $\mathbf{E}_\alpha^e = \partial_0 \mathbf{A}_\alpha^e - \partial_\alpha A_0^e$  represent the external magnetic flux and external electric field strength, respectively. Here,  $J_0^{2\pi} \equiv \epsilon^{\alpha\beta} \Delta_\alpha m_\beta \in \mathbb{Z}$  denotes the number of  $2\pi$  vortices in the holon condensate, and  $\mathbf{J}_\alpha^{2\pi} \equiv -\epsilon^{\alpha\beta} \partial_0 m_\beta \in \mathbb{Z}$  represents the current of the  $2\pi$  vortices. In other words, Eq.(9) corresponds to the fact that in the original holon language, each vortex with  $J_0^{2\pi} = \pm 1$  has a phase winding  $\pm 2\pi$ , while each spinon carries a half-vortex with a phase winding  $\pm\pi$ , known as the spinon-vortex [49, 50].

In the ground state, when all vortices are in the confined phase [53], the superconducting phase coherence is realized with  $\Phi^e = 0$  in Eq.(9) (i.e., the Meissner effect). Here the  $b$ -spinons are in the RVB pairing state according to Eq. (2) and the  $2\pi$  vortices of  $J_0^{\text{vor}} = \pm 1$  are also ‘‘confined’’ in vortex-antivortex pairs. In such an SC phase, a single spinon cannot be present in the bulk, but an  $S = 1$  excitation (totally with  $\pm 2\pi$  vortex due to the double spinons) can be made since a  $\mp 2\pi$  vortex of  $J_0^{\text{vor}}$  can be always bound to the  $S = 1$  excitation to make the total  $\Phi^e = 0$  in Eq. (9). A minimal flux quantization condition of  $\Phi^e = \pi$  ( $= hc/2e \equiv \phi_0$  if the full units are restored) can be realized in Eq. (9) with a single  $b$ -spinon trapped at the magnetic vortex core. The thermally excited free (unpaired)  $b$ -spinons can eventually destroy the Meissner effect with a uniform magnetic field penetrating the bulk according to Eq. (9), which disorders the SC phase coherence and leads to a Kosterlitz–Thouless (KT) like phase transition at [cf. more details in Appendix. B and Ref. 53]

$$T_c \approx E_s/3k_B, \quad (11)$$

where  $E_s$  is the lowest excited energy of the  $b$ -spinons, to be elaborated below.

At  $T$  slightly above  $T_c$ , i.e., the lower PG regime, the conventional  $2\pi$  vortices may remain well confined (vortex-antivortex paired) as their unpaired configuration would cost more free energy than that of the free  $\pi$ -spinon-vortices. To the leading order of approximation, one may then only focus on the spinon-vortex composites without considering the free  $2\pi$  vortices in Eq. (9) and Eq. (10) unless the temperature is much higher than  $T_c$  [50]. Note that a conventional  $2\pi$  vortex can be still bound to a spinon to merely change the vorticity sign of the associated vortex as mentioned above. Namely, the low-energy elementary excitations consist of four types of excited (unpaired)  $b$ -spinons trapped in the vortex cores with quantum numbers of  $\sigma = \pm 1$  and  $\nu = \pm 1$ , where  $\sigma$  is the spin index and  $\nu$  denotes the chirality of the vortex [illustrated on the right-hand-side of Fig. 3(b)]:

$$\sum_\sigma \sigma n_{i\sigma}^b - 2J_0^{2\pi}(i) \Rightarrow \sum_\nu \nu n_{i\sigma\nu}^b, \quad (12)$$

$$\mathbf{J}_\alpha^{\text{spin}}(i) - 2\mathbf{J}_\alpha^{2\pi}(i) \Rightarrow \sum_\nu \nu \mathbf{J}_\alpha^\nu(i) \equiv \mathbf{J}_\alpha^{\text{vor}}(i), \quad (13)$$

where  $n_{i\sigma\nu}^b$  denotes the number of excited free spinons with spin index  $\sigma$  and vorticity  $\nu$ , and  $\mathbf{J}_\alpha^{\text{vor}}$  denotes the

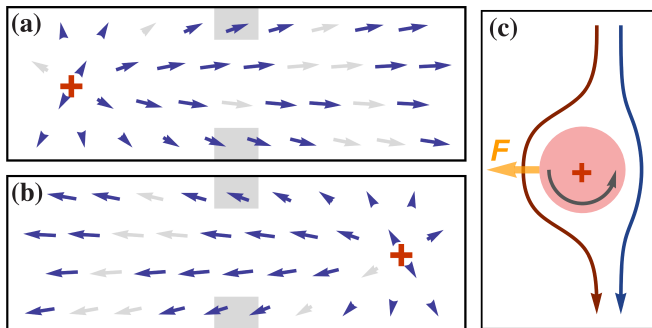


FIG. 2. Schematic illustration of the spinon-vortex motion from one side of the sample [(a)] to the other [(b)]. This traverse along the horizontal direction results in a phase difference between the two opposite sides (indicated by grays) along the vertical direction changes by a  $\pm 2\pi$  continuously, leading to an electric field given in Eq. (15). Here the vortex core is denoted by a red “+” symbol, while the background local phases are represented by blue arrows; (c) The currents flowing along the two sides of a spinning entity, represented by a red disk (the arrow within the disk marks the direction of rotation). Here the red current exhibits a higher velocity compared to its blue counterpart, leading to a “Magnus” force  $F$  exerting on the spinning entity (yellow arrow) as a fluid-dynamic interpretation of Eq. (16).

currents of the spinon-vortices, with  $\mathbf{J}_\alpha^{\nu=\pm}$  representing the spinon current with  $\pm$  chirality. Correspondingly, the equations of motion Eq. (9) and Eq. (10) of the mutual Chern-Simons gauge description reduce to the following forms

$$\sum_\nu \nu n_{i\sigma\nu}^b = -\pi^{-1} \Phi_i^e, \quad (14)$$

$$\mathbf{J}_\alpha^{\text{vor}}(i) = -\pi^{-1} \epsilon_{\alpha\beta} \mathbf{E}_\beta^e(i), \quad (15)$$

Here, Eq. (14) is actually the “chirality-neutral” condition, and Eq. (15) indicates that the current of the spinon-vortices  $\mathbf{J}_\alpha^{\text{vor}}$  along one direction is induced by an external electric field along the perpendicular direction. Physically, the latter case can be interpreted as the steady vortex motion resulting in a  $2\pi$  “phase slip” of the charge field between the opposite sides of perpendicular to the motion direction [cf. Fig. 2(a) and (b)], and thereby generating an electric field, namely the Nernst effect (see in section IV D 1).

Finally, the holon current  $\mathbf{J}^h$  corresponds to the charge current, which can be denoted by  $\mathbf{J}^e$  in the following. A spinon perceives the gauge field  $\sigma A_\mu^h$  in Eq. (1), which results in Eq. (7) where  $\mathbf{E}^h$  is an effective “electric” field acting on the spinon of spin  $\sigma = 1$ , which also denotes the vorticity of the original spinon-vortex composite. Note that a spinon-vortex of  $\sigma = -1$  should experience an opposite force for the same direction of  $\mathbf{J}^e$ . Now such a spinon-vortex can be bound to a  $\pm 2\pi$  vortex to change its vorticity to  $\nu = \pm$ , which becomes independent of  $\sigma$  as given in Eq. (14). The force acting on the spinon-vortex of  $\nu = +$  may then denoted by  $\mathbf{E}^{\text{vor}}$  such that Eq. (7) is

rewritten as:

$$\mathbf{J}_\alpha^e = \pi^{-1} \epsilon_{\alpha\beta} \mathbf{E}_\beta^{\text{vor}}. \quad (16)$$

Physically, such force acting on the vortex induced by the charge current along a direction perpendicular to it can be understood by drawing an analogy with the well-known “Magnus effect” [54] in fluid dynamics, illustrated in Fig. 2(c). In this semi-classical picture, a spinning object (analogous to the vortex) moving through a fluid (representative of the charge current) experiences a lateral force. This force arises from the differential fluid velocity on opposite sides of the spinning object, pushing it in a direction perpendicular to its motion.

Lastly, it is important to emphasize that the relationships given by Eq. (15) and Eq. (16) reflect the well-established concept of boson-vortex duality [55, 56]. Within this framework, the charge and vortex degrees of freedom can be interchanged, highlighting their mutual duality in the described context.

### III. SPINON TRANSPORT

In the mutual Chern-Simons gauge description outlined above, the holon condensation will define the so-called lower PG phase, which is also known as the spontaneous vortex phase (SVP) as the free  $b$ -spinons carry  $\pm\pi$ -vortices. It reaches an intrinsic superconducting phase coherence at a lower critical temperature  $T_c$ . As the basic elementary excitation, the  $b$ -spinon will dictate the lower PG or the SVP phase as well as the superconducting instability at  $T_c$ . The main task in this section is to explore the transport of the  $b$ -spinons, which can expose the physical consequences of the underlying mutual Chern-Simons gauge structure that the  $b$ -spinon is subjected to.

#### A. Spinon excitation spectrum

At the mean-field level, according to Eq. (4), the  $b$ -spinons in  $L_s$  experience a uniform static gauge flux  $\delta\pi$  flux per plaquette as the holons are condensed with  $\langle n_i^h \rangle = \delta$ , which gives rise to a Landau level like energy spectrum  $E_m(\mathbf{k})$ , with the lowest excited sector (LES) at  $E_s$ , as illustrated in Fig. 3(a) in the case of  $\delta = 0.2$  (with  $\delta \equiv 2p/q$  and  $p, q \in \mathbb{Z}$  such that  $p = 1$  and  $q = 10$ ).

In the presence of a perpendicular external magnetic field  $B^e$ , the spinon energy spectrum becomes [cf. more details in Appendix. B]

$$\tilde{E}_{m\sigma\nu}(\mathbf{k}) \equiv E_m(\mathbf{k}) + \sigma \frac{1}{2} g \mu_B B^e + \nu \bar{A}_0^h \quad (17)$$

where the second term on the right is the usual Zeeman splitting for a spin-1/2 with the g-factor (usually taken as 2). The third term originated from the temporal gauge  $A_0^h$ , which results in  $iA_0^h \rightarrow \bar{A}_0^h$  in Eq. (2) following a

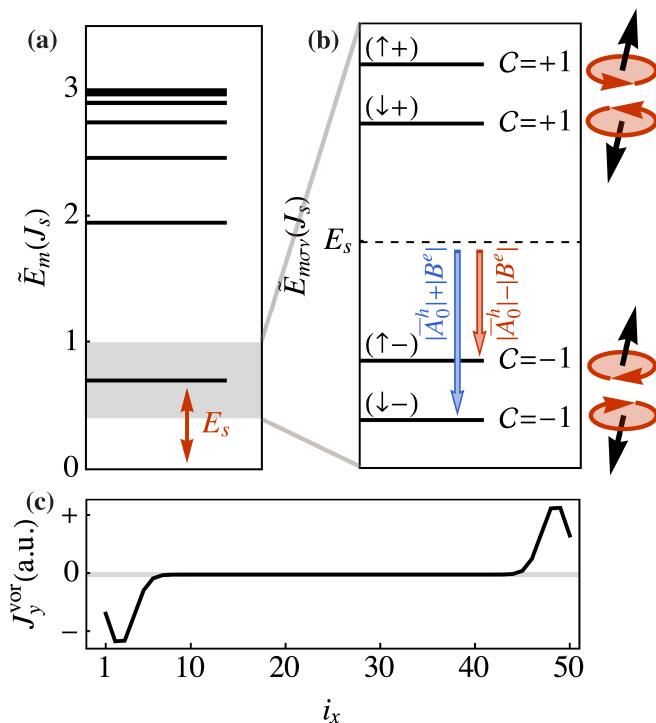


FIG. 3. (a) The spinon energy levels  $\tilde{E}_m$  (at  $\delta = 0.2$ ). The lowest excitations have an energy gap  $E_s$  indicated by the red arrow; (b) The energy splitting of the lowest excitation level in the presence of a perpendicular magnetic field  $B^e$ . This corresponding window is marked by the gray region in (a). Each energy level in (b) is labeled with the quantum number  $(\sigma\nu)$ , with a corresponding diagram, i.e., a spinon trapped in the charge vortex core, illustrated on the right-hand side. Here the Chern number  $C$  and the splitting energy are also indicated; (c) The distribution of the vortex current  $j_y^{\text{vor}}(i)$  along the  $y$  direction in the ground state, which is calculated on a sample with a periodic boundary condition along the  $y$  direction and an open boundary condition along the  $x$  direction. The length of the sample in the  $x$  direction is  $N_x = 50$ .

Wick rotation to enforce the constraint Eq. (14) at  $B^e \neq 0$ .

The mean-field effective Hamiltonian for the spinon-vortex composite may be written as  $\tilde{H}_s = \sum_{m\sigma\nu\mathbf{k}} \tilde{E}_{m\sigma\nu}(\mathbf{k}) \tilde{n}_{m\sigma\nu}^b(\mathbf{k}) + E_0$  with  $\tilde{n}_{m\sigma\nu}^b(\mathbf{k})$  denoting the number of the spinon-vortices as the elementary excitations and  $E_0$  as the ground state energy. As the external magnetic field  $B^e$  is much weaker than the internal fictitious field  $B^h = \delta\pi/a^2$  (with  $a = 3.8\text{\AA}$  as the lattice constant), its effect mainly introduces a minor splitting via the last two terms in  $\tilde{E}_{m\sigma\nu}$ . When the temperature is not too high above  $T_c$  [note that  $E_s$  can be related to  $T_c$  in Eq. (11) explicitly], it is reasonable to project the Hilbert space into the LES around  $E_m(\mathbf{k}) = E_s$ , which is split as shown in Fig. 3(b) [57]. The mean-field parameter  $\bar{A}_0^h$  can be explicitly determined by enforcing the constraint Eq. (14) at  $B^e \neq 0$ , which is illustrated in Fig. 4(a), and

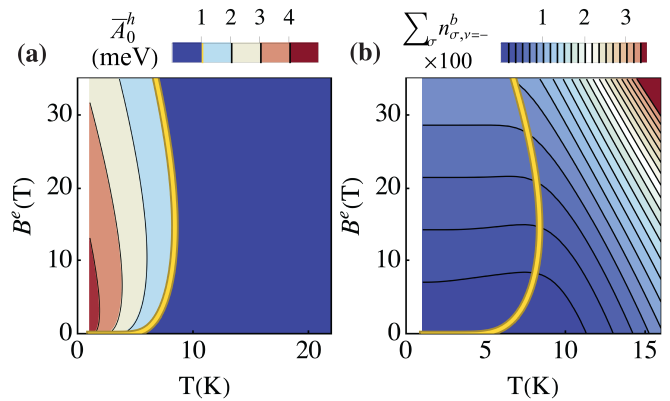


FIG. 4. (a) The evolution of  $\bar{A}_0^h$  with respect to temperature  $T$  and magnetic field  $B^e$ ; (b) The corresponding particle number of excited spinons,  $\sum_{\sigma} n_{\sigma,\nu}^b$ , versus  $T$  and  $B^e$  for a given chirality at lower energy. Here the two distinct temperature regions with different behavior are separated by the yellow line.

the corresponding low-energy excited spinon number  $\sum_{\sigma} n_{\sigma,\nu}^b$  in the LES is displayed in Fig. 4(b). Both figures indicate the existence of two distinct temperature regions, separated by the yellow lines in Fig. 4. In the high-temperature region, the effect of  $\bar{A}_0^h$  on the free spinon number is relatively small due to its small energy compared to  $E_s$ . On the other hand, at low temperatures,  $\bar{A}_0^h$  dominates the lowest-energy excited level, causing the particle number of spinons to correlate linearly with the magnitude of the external field, but remain independent of temperature. The excited spinons will play a significant role in the transport behavior of the lower PG phase.

## B. Transverse transport coefficients

Importantly, due to the gauge field  $B^h$ , the  $b$ -spinon spectrum  $\tilde{E}_{m\sigma\nu}$  carries nontrivial Berry curvatures  $\Omega_{m\sigma\nu}(\mathbf{k}) = i\nabla_{\mathbf{k}} \times \langle u_{m\sigma\nu,\mathbf{k}} | \nabla_{\mathbf{k}} | u_{m\sigma\nu,\mathbf{k}} \rangle$ , with  $|u_{m\sigma\nu,\mathbf{k}}\rangle$  being the periodic part of the Bloch waves corresponding to the energy  $\tilde{E}_{m\sigma\nu}(\mathbf{k})$ . The nonzero Chern number  $C_{m\sigma\nu} = 2\pi \sum_{\mathbf{k}} \Omega_{m\sigma\nu}^z(\mathbf{k})$  for each band within the LES is shown in Fig. 3(b), indicating that the sign of the Chern number depends solely on the chirality of the  $b$ -spinons, leading to  $\sum_{m \in \text{LES}} C_{m\sigma\nu} = \nu$  [58]. Physically, this is because the direction of the intrinsic magnetic field  $B^h$  perceived by the spinons is solely determined by their vorticity sign.

To study the transport properties for  $b$ -spinons, we base our approach on the semiclassical theory, analogous to the quantum Hall effect in electron systems [59]. We consider the  $b$ -spinon wave packet with a relatively determined center and momentum  $(\mathbf{r}, \mathbf{k})$  with an intrinsic size, determined by the ‘‘cyclotron length’’  $a_c = a/\sqrt{\pi\delta}$  [53]. The dynamics of such a wave packet is described by

the semiclassical equation of motion, which includes the topological Berry phase term [59]:

$$\dot{\mathbf{r}} = \frac{1}{\hbar} \frac{\partial \tilde{E}_{m\sigma\nu}(\mathbf{k})}{\partial \mathbf{k}} - \dot{\mathbf{k}} \times \boldsymbol{\Omega}_{m\sigma\nu}(\mathbf{k}) \quad (18)$$

where  $\hbar\dot{\mathbf{k}} = -\nabla U(\mathbf{r})$ , and  $U(\mathbf{r})$  is a confining potential that exists only near the boundary of the sample, which prevents the spinon wave packet from exiting the sample. On the edge along the  $x$  direction, for example, the non-trivial Berry curvature produces an anomalous velocity  $\dot{\mathbf{k}} \times \boldsymbol{\Omega}_{m\sigma\nu}(\mathbf{k}) = -\hbar^{-1} \partial_y U(\mathbf{r}) \Omega_{m\sigma\nu}^z(\mathbf{k}) \hat{x}$  in Eq. (18). Physically, this anomalous velocity arises from the fact that  $b$ -spinon perceives an intrinsic ‘‘Lorentz force’’ due to the uniform gauge field  $B^h$  from the holons, the sign of which depends on the vorticity. Therefore,  $b$ -spinon undergoes a cyclotron motion in the bulk and a skipping orbit along the edge of the sample, as illustrated in Fig. 1(b). It is crucial to note that both spinons carrying opposite chirality flow along the boundary. This scenario is reminiscent of the quantum spin Hall effect [35, 36], where the electrons at the boundary carry opposite spin directions. Also, in contrast to the chiral spin liquid with chiral edge modes [60, 61], our effective description [as referenced in Eq. (1)-(3)] maintains time-reversal symmetry. Here, to draw parallels and distinctions from previously observed phenomena, the behavior of the neutral spin within our framework may be termed the bosonic ‘‘anomalous vortex Hall’’ effect, which underscores the vortex edge current arising from the internal fictitious magnetic field. On the other hand, in the case of equilibrium, all the edge current in the sample cancels between one edge and the opposite edge shown in Fig. 1(c), resulting in no net current.

In the presence of either a spatially varying chemical potential  $\mu$  or temperature  $T$ , a net edge current is contributed by the anomalous velocity of  $b$ -spinon, as shown in Fig. 1(b)-(d). For instance, when there is a temperature gradient and a chemical potential gradient in the  $y$  direction, the linear response of the chiral spinon current  $\mathbf{J}^\nu$  and the heat current  $\mathbf{J}_Q^\nu$ , with their respective chirality  $\nu$ , can be expressed as [62–65]

$$\begin{bmatrix} \mathbf{J}_x^\nu \\ (\mathbf{J}_Q^\nu)_x \end{bmatrix} = \mathbf{L}^{\text{xy},\nu} \begin{bmatrix} -\nabla_y \mu \\ T \nabla_y \frac{1}{T} \end{bmatrix}, \quad (19)$$

Here,  $\mathbf{L}^{\text{xy},\nu}$  signifies a  $2 \times 2$  matrix that represents the transverse transport coefficients. The parameter  $\nu = \pm$  distinguishes between the different chiralities of spinon. The matrix elements are given by

$$\begin{aligned} L_{ij}^{\text{xy},\nu} &\approx -\frac{1}{\hbar V \beta q} \sum_{m \in \text{LES}} \sum_{\sigma \mathbf{k}} c_q(n_{m\sigma\nu}^b) \Omega_{m\sigma\nu}^z(\mathbf{k}) \\ &= -\frac{\nu}{\hbar \beta q 2\pi} \sum_{\sigma} c_q(n_{\sigma\nu}^b) \end{aligned} \quad (20)$$

where  $i, j = 1, 2$ ,  $c_q(x) \equiv \int_0^x (\log \frac{1+t}{t})^q dt$ ,  $q = i + j - 2$ , and  $n_{m\sigma\nu}^b = 1 / (e^{\beta \tilde{E}_{m\sigma\nu}} - 1)$  is the bosonic distribution function for  $b$ -spinons, which is independent of momentum, because  $\tilde{E}_{m\sigma\nu}$  is the flat Landau-level band in

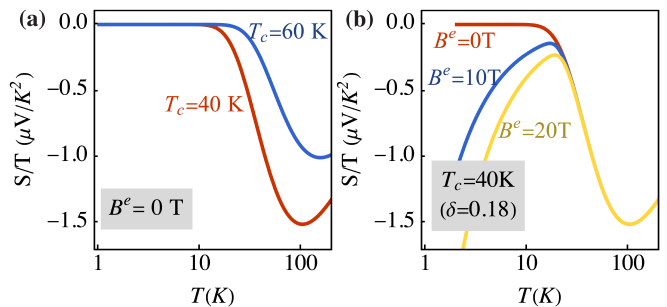


FIG. 5. The evolution of the Seebeck coefficient with respect to temperature is depicted in (a), without the influence of a magnetic field, and in (b), at a doping density  $\delta = 0.18$  and a critical temperature  $T_c = 40\text{K}$ .

our case. Note that in Eq. (20), as an approximation, we only sum over within the LES and use the relation  $\sum_{m \in \text{LES}} C_{m\sigma\nu} = 2\pi \sum_{\mathbf{k}} \Omega_{m\sigma\nu}^z(\mathbf{k}) = \nu$ . In the following, we will investigate various transport measurements associated with the transverse transport coefficients  $L_{ij}^{\text{xy}}$  in Eq. (20) (for simplicity we shall drop the superscript  $xy$  in the following such that  $L_{ij}^{\text{xy},\nu} \rightarrow L_{ij}^\nu$ ).

## IV. EXPERIMENTALLY TESTABLE CONSEQUENCES

### A. Thermopower

As illustrated in Fig. 1(c), due to the internal flux  $B^h$ , the  $b$ -spinons with opposite vorticities will propagate in opposite directions along the edges of the sample, such that there is a *net* vortex current at each edge along the  $x$  direction, which would be canceled out by the opposite edges at  $\nabla_y T = 0$ . Now let us consider a temperature gradient  $\nabla_y T$  applied along the  $y$  direction. As depicted in Fig. 1(d), the vortex current on one side of the boundary will be larger than on the higher- $T$  side, which will result in a finite total vortex current along the  $x$  direction. Noting that  $\mathbf{J}_x^{\text{vor}} = \mathbf{J}_x^{\nu=+} - \mathbf{J}_x^{\nu=-}$ , where  $\mathbf{J}_x^{\nu=\pm}$  represents the spinon current with  $\pm$  chirality [50] as given by  $\mathbf{J}_x^{\nu=\pm} = L_{12}^{\nu=\pm} (T \partial_y \frac{1}{T})$  according to Eq. (20). Furthermore, according to Eq. (15), the net vortex current  $\mathbf{J}_x^{\text{vor}}$  along the  $x$  direction can induce an electric field  $\mathbf{E}_y^e$  along the  $y$  direction (similar to the contribution to the Nernst effect as to be discussed later), which will contribute to a finite thermopower, with the Seebeck coefficient given by

$$S \equiv \frac{\mathbf{E}_y^e}{\nabla_y T} = -\frac{k_B \phi_0}{2\pi \hbar} \sum_{\sigma\nu} c_1(n_{\sigma\nu}^b) \quad (21)$$

where  $c_1(x) \equiv (1+x) \ln(1+x) - x \ln x$ . Thus such a contribution of the  $b$ -spinon to the Seebeck coefficient is determined by the number of the excited  $b$ -spinons,  $n_{\sigma\nu}^b$ , which in turn is essentially governed by the lowest excited energy scale in Eq. (17) at low temperatures.

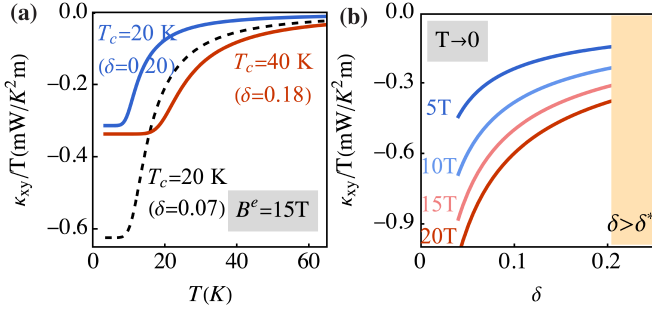


FIG. 6. (a) The temperature evolution of the thermal-Hall coefficient when  $B = 15T$ . The solid line represents the case in the overdoped regime, while the dashed line signifies the case in the underdoped regime. (b) The doping evolution of the thermal-Hall coefficient as the temperature approaches zero. The thermal-Hall effect is predicted to revert to conventional Fermi liquid behaviors when the doping density  $\delta$  is greater than the critical density  $\delta^*$ , as indicated by the yellow region.

A typical quantitative temperature-dependence of the Seebeck coefficient  $S$  calculated using Eq. (21) is shown in Fig. 5 at zero magnetic fields [(a)] and at finite  $B$ 's [(b)] in the overdoped regime. The overall  $T$ - and  $B$ -dependence and magnitude here are in agreement with the experimental measurements in the optimal and overdoped cuprates [37, 38].

## B. Thermal Hall

Similarly, with a temperature gradient along the  $y$  direction, we can also evaluate the net thermal current  $(\mathbf{J}_Q)_x = (\mathbf{J}_Q^{\nu=+})_x + (\mathbf{J}_Q^{\nu=-})_x$  along the  $x$  direction, as illustrated in Fig. 1(e). Here,  $\mathbf{J}_Q^{\nu=\pm}$  represents the thermal current contributed by spinons with  $\pm$  chirality, expressed as  $(\mathbf{J}_Q^{\nu=\pm})_x = L_{22}^{\nu=\pm} (T \partial_y \frac{1}{T})$ , according to Eq. (20). The thermal Hall conductivity is then given by[62–65]:

$$\kappa^{xy} \equiv -\frac{J_Q}{\nabla_y T} = -\frac{k_B^2 T}{2\pi\hbar} \sum_{\nu\sigma} \nu c_2(n_{\nu\sigma}^b) \quad (22)$$

where  $c_2(x) = (x+1)(\ln \frac{1+x}{x})^2 - (\ln x)^2 - 2\text{Li}_2(-x) - c$ , with  $\text{Li}_2(z)$  being the polylogarithm function, and  $c = \pi^2/3$  is a constant ensuring that  $\kappa^{xy}$  does not diverge as  $T \rightarrow \infty$ .

It is crucial to note that, in the absence of an external magnetic field, the vanishing of both  $B^e$  and  $\bar{A}_0^h$  leads to the degeneracy of  $\tilde{E}_{m\sigma\nu}$  with respect to chirality  $\nu$ , resulting in a zero value for  $\kappa^{xy}$  in Eq. (22) due to the summation over  $\nu$ . Essentially, this outcome stems from the fact that the thermal current with opposite chirality flows in opposite directions along a boundary. Therefore, the preservation of total chirality to zero in a sample without an external magnetic field results in complete cancellations for the thermal current. Conversely, in the

presence of an external magnetic field  $B^e$ , according to Eq. (14), the total chirality for  $b$ -spinons becomes finite, leading to a net thermal current along the boundary.

As a result, the evolution of thermal Hall conductivity  $\kappa^{xy}$  obtained by Eq. (22) with respect to temperature is depicted in Fig. 6(a). This evolution aligns with experimental results in terms of magnitude[8–10], and it exhibits distinct behaviors across different temperature regions. In the high-temperature region, following the discussion about Eq. (17),  $n_{\nu\sigma}^b$  is not sensitive to  $\bar{A}_h^0$ , leading to  $\kappa^{xy}/T = -\frac{B^e k_B^2}{\hbar\pi\phi_0\delta} \left(\frac{3T_c}{T}\right)^2$  [Eq. (11) is used here]. On the other hand, in the low-temperature region where spontaneous (thermally excited) vortices are absent, Eq. (14) reduces to  $\sum_{\sigma} n_{\sigma\nu=-}^b \approx B^e a^2/2\phi_0\delta$ . Here, all other energy levels remain unoccupied, leading to  $\kappa_{xy}/T \rightarrow -k_B^2 c_2(B^e a^2/2\phi_0\delta)/\hbar\pi$  as  $T$  approaches 0. The doping evolution of  $\kappa_{xy}/T$  near zero temperature is presented in Fig. 6(b). This evolution reveals enhanced signals in the underdoped regimes, corroborating the experimental measurements[8–10]. Physically, this is because, under low doping conditions, the degeneracy of the lowest Landau level of the spinons is reduced due to the small intrinsic magnetic field strength  $\delta\pi$ . This reduction in degeneracy increases the average Berry curvature, denoted as  $\Omega_{m\sigma\nu}$ , experienced by each spinon, which enhances the anomalous velocity at the boundary, as indicated by Eq. (18). Therefore, the thermal Hall effect becomes more pronounced under low doping. However,  $\kappa_{xy}/T$  will not truly diverge at  $\delta \rightarrow 0$ , due to the fact that the uniform holon condensation will either be broken down or form smaller domain structures when it is deeply in the AFM long-range ordered phase [10]. Our results for the thermal Hall conductivity differ from the bosonic scaling law in Ref. 18, where Zhang et al. utilized the gapless bosons with a power-law Berry curvature. Here we emphasize that the intrinsic flux  $B_h$  leads to the Landau level structure, with the gap of the spinon-vortices constrained by Eq. (14), resulting in a decreasing gap as the temperature drops as illustrated in Fig. 4. Notably, within the pseudogap regime, the role of the spinon-vortex is to neutralize the external magnetic field. Consequently, its Hall response is in the opposite direction compared to the charged quasiparticles manifesting in the Fermi liquid regime. This elucidates the observed sign change of the thermal Hall as the doping transitions into the pseudogap phase [10].

It is important to note that our case does not involve the spontaneous breaking of time-reversal symmetry, a necessary condition to avoid the emergence of a hysteretic behavior not observed experimentally. Furthermore, according to Eq. (14), the total chirality carried by  $b$ -spinons is induced linearly with the applied magnetic field. This results in the linear- $B$  dependence of  $\kappa^{xy}$  in both distinct temperature regions, which aligns with the experimental measurement[8–10].

### C. Hall Effect

According to Eq. (16), driving a charge current  $\mathbf{J}_x^e$  along the  $x$  direction induces an electric field  $\mathbf{E}_y^{\text{vor}}$  applied to the vortex along the  $y$  direction. This electric field acts as the chemical potential gradient  $\mathbf{E}_y^{\text{vor}} = -\nabla_y \mu$  in Eq. (19). Since the  $\pm$  vortices perceive the  $\mathbf{E}_y^{\text{vor}}$  in opposite directions, the response spinon current  $\mathbf{J}_x^{\nu=\pm} = L_{11}^{\nu=\pm} \mathbf{E}_y^{\text{vor}}$  leads to the vortex current  $\mathbf{J}_x^{\text{vor}} = \sum_{\nu} \nu L_{11}^{\nu=\pm} \mathbf{E}_y^{\text{vor}}$ . From Eq. (15), this induced vortex current further generates an electric field  $\mathbf{E}_y^e$  along the  $y$  direction, culminating in the Hall effects as illustrated in Fig. 1(f). Therefore, the obtained Hall coefficient  $R_H$  is given by

$$R_H \equiv \frac{\mathbf{E}_y^e d}{\mathbf{J}_x^e B^e} = \frac{a^2 d}{e \delta}, \quad (23)$$

where  $d$  denotes the lattice constants along the  $z$ -axis. We also employ the relation  $c_0(x) = x$  and Eq. (14).

Therefore, the Hall number calculated by Eq. (23) is given by  $n_H = a^2 d / e R_H = \delta$ , which is consistent with the experimental results [3, 4]. Significantly, there exists a long-standing experimental puzzle wherein the charge carrier, as measured by the Hall number, correlates with the doped hole density  $\delta$  in the PG. This contrasts with the  $1 + \delta$  measurement derived from the Fermi surface area observed through angle-resolved photoemission spectroscopy (ARPES) [66–68], seemingly deviating from the Luttinger sum rule. Our results offer a compelling explanation: chiral spinons primarily contribute to the Hall effects. In contrast, the entities forming the Fermi surface — Landau quasiparticles — display a negligible Hall effect signal due to their partially diminished weight (Fermi arcs) in the PG phase.

Note that the Hall effect in this framework is primarily attributed to the edge states of chiral spinons. At elevated temperatures, the local phase coherence of holons can become further disrupted, rendering them incapable of sustaining condensation when the distance between spinon-vortices becomes comparable to that of the doped holes. In such a scenario, chiral spinons no longer experience the uniform static gauge flux emitted by holons, and thus cannot sustain their complete edge states. Consequently, the contribution of such channels to the Hall effect would diminish as the temperature rises, consistent with experimental measurements [3, 4].

### D. Other Properties of Spinon-vortices

In the above subsections, the effects produced by the transverse motion of the chiral spinons with the MCS gauge structure have been explored. It is noted that the effects of the longitudinal motion of the same chiral spinons have been already studied previously [49, 50, 69]. Since the  $b$ -spinons are the elementary excitations that dictate the lower PG phase, for the sake of completeness,

in the following we briefly discuss additional phenomena associated with the  $b$ -spinons.

#### 1. Nernst Effect

When a temperature gradient is applied along the  $y$  direction, our attention shifts from the transverse transport motion detailed in Eq. (19), to the longitudinal drift motion of spinons. To explore this, we introduce a viscosity constant,  $\eta_s$ , which allows us to determine the drift velocity  $\mathbf{v}^b$  of chiral spinons using the equation  $s_\phi \nabla T = -\eta_s \mathbf{v}^b$ , where  $s_\phi$  denotes the transport entropy carried by a spinon vortex. It's important to note that spinons of both chiralities are driven by a temperature gradient in the same direction along the  $x$ -axis, with the velocity being the same  $\mathbf{v}^b$ .

In the presence of an external magnetic field  $B^e$ , a vortex current  $\mathbf{J}_y^{\text{vor}}$  is induced along the  $y$ -axis. As discussed in the thermopower section, the vortex current can be further expressed as  $\mathbf{J}^{\text{vor}} = (n_{\sigma\nu=+} - n_{\sigma\nu=-}) \mathbf{v}^b$ , where the amplitude is proportional to the external magnetic field as per the chirality “neutrality” condition Eq. (14). This vortex current  $\mathbf{J}_y^{\text{vor}}$  induces an electric field  $\mathbf{E}_x^e$  along the  $x$ -axis, as dictated by Eq. (15). This corresponds to the Nernst effects, with the signal defined by [49]:

$$e_N = \frac{\mathbf{E}_y}{|\nabla_x T|} = B^e \frac{s_\phi}{\eta_s}. \quad (24)$$

To eliminate the viscosity  $\eta_s$  in Eq. (24), let us consider the longitudinal resistivity  $\rho_e$  resulting from the drift motion of chiral spinons. According to Eq. (16), driving a charge current  $\mathbf{J}_x^e$  along the  $x$  direction induces an “electric field”  $\mathbf{E}_y^{\text{vor}}$  on the vortex. In contrast to the temperature gradient,  $\mathbf{E}_y^{\text{vor}}$  prompts spinons of both chiralities to drift in opposite directions along the  $y$ -axis, in accordance with the relation  $\mathbf{E}_y^{\text{vor}} = \pm \eta_s / \hbar c \mathbf{v}_y^b$ . This results in a vortex current  $\mathbf{J}^{\text{vor}} = n_{\sigma\nu=+}^b \mathbf{v}^b - n_{\sigma\nu=-}^b (-\mathbf{v}^b) = n^b \mathbf{v}^b$ , where  $n^b = \sum_{\sigma\nu} n_{\sigma\nu}^b$  is the total number of free  $b$ -spinons. Next, as derived from Eq. (15), such vortex current  $\mathbf{J}_y^{\text{vor}}$  induces the electric field  $\mathbf{E}_x^e$  along the  $x$  direction, leading to the longitudinal resistivity

$$\rho_e = \phi_0^2 n_\nu / \eta_s, \quad (25)$$

where the contribution from quasiparticles are not included in this analysis. Lastly, the challenging-to-calculate viscosity  $\eta_s$  is eliminated, yielding [49]:

$$\alpha_{xy} \equiv \frac{e_N}{\rho} = \frac{B^e a^2 s_\phi}{\phi_0^2 n_\nu}, \quad (26)$$

where  $\alpha_{xy}$  is the quantity introduced in Ref. 39. Within our framework, a unique aspect that sets it apart from a conventional BCS superconductor is the presence of a free  $S = 1/2$  moment locked with the vortex core, which gives rise to the “transport entropy” [40]  $s_\phi =$



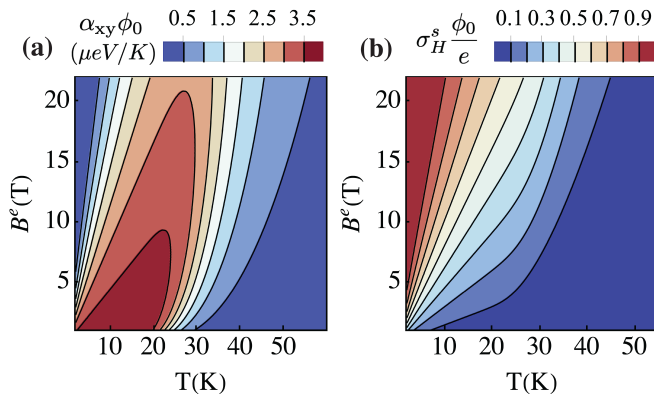


FIG. 7. The temperature and magnetic field contour plot of  $\alpha_{xy} \equiv eN/\rho$  (a) and the spin Hall coefficient  $\sigma_H^s$  (b).

$k_B \ln [2 \cosh(\beta\mu_B B^e)] - \beta\mu_B B^e \tanh(\beta\mu_B B^e)$ . The temperature and magnetic-field dependence of  $\alpha_{xy}$  is illustrated in Fig. 7(a). Its magnitude aligns quantitatively with experimental data [39–41], suggesting that the transport entropy due to the free moment in a spinon vortex can accurately replicate the Nernst signal observed experimentally.

### 2. Spin Hall Effect

In the presence of a magnetic field, both the chirality and spin degrees of freedom become polarized through the orbit and Zeeman effects, respectively. In this scenario, a charge current  $\mathbf{J}_x^e$  along the  $x$  direction not only induces a vortex current  $\mathbf{J}_y^{\text{vor}}$  along the  $y$  direction—as previously discussed—but also generates a spin current. The latter can be expressed as  $\mathbf{J}_\alpha^s = (n_{\uparrow+}^b - n_{\downarrow+}^b)\mathbf{v}_\alpha + (n_{\uparrow-}^b - n_{\downarrow-}^b)(-\mathbf{v}_\alpha) = \sum_{\sigma\nu} \sigma\nu n_{\sigma\nu}^b \mathbf{v}_\alpha$ . This results in the generation of a vortex current that accompanies a spin current, with the ratio defined as  $\zeta \equiv J_\alpha^s/J_\alpha^{\text{vor}} = \sum_{\sigma\nu} \sigma\nu n_{\sigma\nu}^b/n^b$ . As a consequence, the PG phase is predicted to exhibit a spin Hall effect, with the coefficient given by [49, 69]:

$$\sigma_H^s \equiv \frac{J_\alpha^s}{\mathbf{E}_\alpha^e} = \frac{e}{\phi_0} \zeta, \quad (27)$$

of which the calculated magnitude is shown in Fig. 7(b).

### 3. Order-to-Order Phase Transition

At the units  $\hbar = c = e = 1$ , Eq. (25) can be recast into a dual form:

$$\sigma_e \sigma_s = \frac{1}{\pi^2}, \quad (28)$$

where  $\sigma_e = 1/\rho_e$  represents the electrical conductance, while  $\sigma_s \equiv \mathbf{J}_\alpha^{\text{vor}}/\mathbf{E}_\alpha^{\text{vor}} = n_v/\eta_s$  denotes the spinon conductance. Essentially, Eq. (28) parallels the boson-vortex

duality [55, 56], in which both the Cooper pair and the superconductivity vortex perceive each other as vortices. As such, when one is in a superfluid state, the other resides in an insulating state.

Within the context of our work, the spinon (holon) carries the holon (spinon) vortex, thereby uniquely associating all vortices with quantum numbers. Based on Eq. (28), the superconductivity phase characterized by  $\sigma_e \rightarrow \infty$ , corresponds to an insulating phase for the spinon with  $\sigma_s \rightarrow 0$ . Moreover, when spinon condenses with  $\sigma_s \rightarrow \infty$ , indicating the establishment of antiferromagnetic long-range order, it triggers the proliferation of holon vortices, thereby resulting in an insulating phase in charge, i.e.,  $\sigma_e \rightarrow 0$ . This sequence represents a novel type of “order-to-order” phase transition, widely investigated under the rubric of “deconfined quantum critical point” (DQCP) [70–72].

### 4. Relation between $T_c$ and resonance energy in INS

The dynamic spin susceptibility, as observed via inelastic neutron scattering (INS), reveals the transition of the gapless spin-wave [73, 74] at the antiferromagnetic (AFM) wave vector  $(\pi, \pi)$  to a gapped state upon disruption of the AFM long-range order. This spin excitation also manifests a resonance-like mode [44, 75–80] characterized by energy  $E_g$ , demonstrating a peak in the spin spectrum weight. When deviating slightly from the momentum  $(\pi, \pi)$ , the resonance mode bifurcates and spans both higher and lower energies, resulting in the well-documented hourglass-shaped spectrum [81–86].

Within our proposed framework, the predominant low-lying spin spectrum weight originates from the LES of chiral spinons characterized by energy  $E_s$ . Furthermore, the  $S = 1$  spin excitation detected by INS is in fact a composite of two  $S = 1/2$  spinons, resulting in the resonance spin mode energy  $E_g = 2E_s$ . A careful analysis [87] further validates that the spinon excitation discussed in our study is consistent with the observed hour-glass spin spectrum.

A key insight is the established relation between the resonance energy  $E_g$  observed in INS and the superconducting critical temperature  $T_c$ . The relation [detailed derivation in Appendix B and Ref. 53] is expressed as:

$$\kappa \equiv \frac{E_g}{k_B T_c} \approx 6.45, \quad (29)$$

which aligns closely with the experimental measurement [42–45]  $\kappa^{\text{exp}} \approx 6$ .

## V. DISCUSSION

One of the key hypotheses on the high- $T_c$  cuprate in a doped Mott insulator approach [1] is that the PG phase is a fractionalized novel state beyond the Landau Fermi-liquid description. In other words, it is the spinon and

holon instead of the Landau quasiparticle that dictate the physics of the PG phase. The transport properties can provide a very powerful test of distinct hypotheses of the elementary excitations and thus the underlying states of matter.

In this work, we have specifically explored the transverse transport of the chiral spinons, which are elementary excitations characterizing the lower PG phase. Here the spinon and holon are subjected to the mutual Chern-Simons gauge structure due to the phase-string effect in a doped Mott insulator, which preserves the time-reversal and parity symmetries in the absence of the external magnetic field. In the so-called lower PG phase, the holons remain Bose-condensed but the superconducting phase coherence is disordered by free spinon excitations until the “confinement” of the spinons below  $T_c$ . The time-reversal symmetry is retained because the opposite spins see the opposite directions of the fluxes and form the RVB pairing in the superconducting ground state. Here the transverse transport refers to the rotational motion of the spinons as the edge chiral currents under the internal statistical fictitious fluxes, which may be regarded as the bosonic “anomalous vortex Hall” effect.

Both the neutral and electric Hall effects are exhibited in the presence of a perpendicular magnetic field. In contrast to the conventional Boltzmann transport of the Landau quasiparticles, the thermopower, thermal Hall, and the Hall effect studied here are all contributed by the chiral spinons, which are further locked with a vortex supercurrent via the mutual Chern-Simons gauge field in generating a transverse electric voltage. The magnitudes of the calculated transverse transport coefficients are intrinsically linked to the resonance-like energy scale of the chiral spinons, which can further determine [53, 87, 88] the SC transition temperature,  $T_c$ , and be detected by the inelastic neutron scattering experiments [44, 75, 78–80]. Previously the longitudinal transport of such chiral spinons has been shown to give rise to the Nernst effect [50], the spin Hall effect [69] as briefly mentioned in Sec. IV D. Additionally, in such a framework, an “order-to-order” phase transition between AFM insulating phase and SC phase is expected in the cuprates, which is worth further investigation in the future to establish a possible relationship with the DQCP [70–72].

It is further noted that the origin of the thermal Hall effect in different studies [12–14], starting from the  $\pi$ -flux fermionic spinons, has been also attributed to the Berry curvatures of the spinon bands. However, without the external magnetic fields, the normal state of spinons [14] is usually conventional or topologically trivial. By contrast, here the external magnetic field merely shifts the balance number of the excited spinons with opposite chirality without changing the internal strong Berry curvatures introduced by the nontrivial topological (mu-

tual Chern-Simons) gauge structure. The latter is intrinsically embedded in the pseudogap regime, describing the long-range entanglement between spin and charge degrees of freedom due to the phase-string effect in the doped Mott insulator. Additionally, some other studies attribute the enhancement of the thermal Hall signal to phonons through some extrinsic mechanisms[15–17]. It should be pointed out that bare phonons are not sensitive to the direction of external magnetic fields, but the experimentally observed thermal Hall coefficient in cuprates depends on the magnetic field component perpendicular to the copper oxide plane [9].

Importantly, all the transport results obtained in this work hinge on the robustness of the chiral spinon excitation, which is protected by the underlying bosonic RVB pairing. However, as the doping further increases beyond a critical point, i.e.,  $\delta > \delta^*$ , the AFM correlation becomes too weak to preserve such an RVB pairing, leading to the breakdown of the pseudogap phase and the restoration of a Fermi liquid with a large Fermi surface [89], as has been suggested experimentally [66–68, 90, 91]. As a result, apparently, the present transport results should collapse with the contribution dominated by the quasiparticle excitations with the full Fermi surface restored in the overdoped regime at low temperatures. For instance, as indicated by experiments, the Hall number should change from  $\delta$  to  $1 + \delta$  [3, 4] and the thermal Hall coefficient should restore the behavior of the Wiedemann-Franz law [10].

Finally, we note that certain experiments have recently detected a signal of the thermal Hall effect along the  $z$ -axis in cuprates [8]. Our current study has been focused on the pure 2D and does not offer a quantitative explanation. We speculate that since the phase-string sign structure underlies the intrinsic Berry curvatures leading to the thermal Hall effect, its existence in any dimensions of a doped Mott insulator which has been rigorously proven [33] before, may be also responsible for the above-mentioned experimental observation beyond 2D. Technically, in realistic materials—stacked copper oxide layers—the interlayer coupling may cause the edge state of the spinons, as described in this paper, to undergo tunneling between different layers. A further study along this line will be worth proceeding elsewhere.

## ACKNOWLEDGMENTS

*Acknowledgments.*— We acknowledge stimulating discussions with Long Zhang, Binghai Yan, Yuanming Lu, and Gang Li. Z.-J.S, J.-X.Z., and Z.-Y.W. are supported by MOST of China (Grant No. 2021YFA1402101).

---

[1] P. A. Lee, N. Nagaosa, and X.-G. Wen, *Rev. Mod. Phys.* **78**, 17 (2006).

[2] B. Keimer, S. A. Kivelson, M. R. Norman, S. Uchida,

- and J. Zaanen, *Nature* **518**, 179 (2015).
- [3] C. Proust and L. Taillefer, *Annu. Rev. Condens. Matter Phys.* **10**, 409 (2019).
  - [4] S. Badoux, W. Tabis, F. Laliberté, G. Grissonnanche, B. Vignolle, D. Vignolles, J. Béard, D. A. Bonn, W. N. Hardy, R. Liang, N. Doiron-Leyraud, L. Taillefer, and C. Proust, *Nature* **531**, 210 (2016), 1511.08162.
  - [5] J. G. Storey, *EPL* **113**, 27003 (2016), 1512.03112.
  - [6] Y.-H. Zhang and S. Sachdev, *Physical Review Research* **2**, 023172 (2020), 2001.09159.
  - [7] A. Nikolaenko, M. Tikhonovskaya, S. Sachdev, and Y.-H. Zhang, *Physical Review B* **103**, 235138 (2021), 2103.05009.
  - [8] G. Grissonnanche, S. Thériault, A. Gourgout, M.-E. Boulanger, E. Lefrançois, A. Ataei, F. Laliberté, M. Dion, J.-S. Zhou, S. Pyon, T. Takayama, H. Takagi, N. Doiron-Leyraud, and L. Taillefer, *Nature Physics* **16**, 1108 (2020), 2003.00111.
  - [9] M.-E. Boulanger, G. Grissonnanche, S. Badoux, A. Alaire, E. Lefrançois, A. Legros, A. Gourgout, M. Dion, C. H. Wang, X. H. Chen, R. Liang, W. N. Hardy, D. A. Bonn, and L. Taillefer, *Nature Communications* **11**, 5325 (2020), 2007.05088.
  - [10] G. Grissonnanche, A. Legros, S. Badoux, E. Lefrançois, V. Zatkó, M. Lizaïre, F. Laliberté, A. Gourgout, J.-S. Zhou, S. Pyon, T. Takayama, H. Takagi, S. Ono, N. Doiron-Leyraud, and L. Taillefer, *Nature* **571**, 376 (2019), 1901.03104.
  - [11] H. Katsura, N. Nagaosa, and P. A. Lee, *Physical Review Letters* **104**, 066403 (2010), 0904.3427.
  - [12] J. H. Han, J.-H. Park, and P. A. Lee, *Physical Review B* **99**, 205157 (2019), 1903.01125.
  - [13] H. Guo, R. Samajdar, M. S. Scheurer, and S. Sachdev, *Physical Review B* **101**, 195126 (2020), 2002.01947.
  - [14] R. Samajdar, M. S. Scheurer, S. Chatterjee, H. Guo, C. Xu, and S. Sachdev, *Nature Physics* **15**, 1290 (2019), 1903.01992.
  - [15] H. Guo and S. Sachdev, *Physical Review B* **103**, 205115 (2021), 2103.02614.
  - [16] H. Guo, D. G. Joshi, and S. Sachdev, *Proceedings of the National Academy of Sciences* **119**, e2215141119 (2022), <https://www.pnas.org/doi/pdf/10.1073/pnas.2215141119>.
  - [17] J.-Y. Chen, S. A. Kivelson, and X.-Q. Sun, *Physical Review Letters* **124**, 167601 (2020), 1910.00018.
  - [18] Y.-f. Yang, G.-M. Zhang, and F.-C. Zhang, *Physical Review Letters* **124**, 186602 (2020), 2001.08385.
  - [19] M. Hirschberger, J. W. Krizan, R. J. Cava, and N. P. Ong, *Science* **348**, 106 (2015).
  - [20] Y. Kasahara, K. Sugii, T. Ohnishi, M. Shimozawa, M. Yamashita, N. Kurita, H. Tanaka, J. Nasu, Y. Motome, T. Shibauchi, and Y. Matsuda, *Physical Review Letters* **120**, 217205 (2018).
  - [21] D. Watanabe, K. Sugii, M. Shimozawa, Y. Suzuki, T. Yajima, H. Ishikawa, Z. Hiroi, T. Shibauchi, Y. Matsuda, and M. Yamashita, *Proceedings of the National Academy of Sciences* **113**, 8653 (2016).
  - [22] S. Jezouin, F. D. Parmentier, A. Anthore, U. Gennser, A. Cavanna, Y. Jin, and F. Pierre, *Science* **342**, 601 (2013).
  - [23] M. Banerjee, M. Heiblum, A. Rosenblatt, Y. Oreg, D. E. Feldman, A. Stern, and V. Umansky, *Nature* **545**, 75 (2017).
  - [24] M. Banerjee, M. Heiblum, V. Umansky, D. E. Feldman, Y. Oreg, and A. Stern, *Nature* **559**, 205 (2018).
  - [25] C. L. Kane and M. P. A. Fisher, *Physical Review B* **55**, 15832 (1997).
  - [26] Z.-Y. Weng, *New J. Phys.* **13**, 103039 (2011).
  - [27] Y. Ma, P. Ye, and Z.-Y. Weng, *New J. Phys.* **16**, 083039 (2014).
  - [28] D. P. Arovas and A. Auerbach, *Phys. Rev. B* **38**, 316 (1988).
  - [29] G. Baskaran, Z. Zou, and P. Anderson, *Solid State Commun.* **63**, 973 (1987).
  - [30] P. W. Anderson, *Science* **235**, 1196 (1987).
  - [31] N. Read and S. Sachdev, *Phys. Rev. Lett.* **66**, 1773 (1991).
  - [32] D. N. Sheng, Y. C. Chen, and Z. Y. Weng, *Phys. Rev. Lett.* **77**, 5102 (1996).
  - [33] K. Wu, Z. Y. Weng, and J. Zaanen, *Phys. Rev. B* **77**, 155102 (2008).
  - [34] X. Lu, J.-X. Zhang, S.-S. Gong, D. N. Sheng, and Z.-Y. Weng, (2023), [arXiv:2303.13498](https://arxiv.org/abs/2303.13498).
  - [35] B. A. Bernevig, T. L. Hughes, and S.-C. Zhang, *Science* **314**, 1757 (2006).
  - [36] M. König, S. Wiedmann, C. Brüne, A. Roth, H. Buhmann, L. W. Molenkamp, X.-L. Qi, and S.-C. Zhang, *Science* **318**, 766 (2007), 0710.0582.
  - [37] R. Daou, O. Cyr-Choinière, F. Laliberté, D. LeBoeuf, N. Doiron-Leyraud, J.-Q. Yan, J.-S. Zhou, J. B. Goodenough, and L. Taillefer, *Phys. Rev. B* **79**, 180505 (2009).
  - [38] M. Lizaïre, A. Legros, A. Gourgout, S. Benhabib, S. Badoux, F. Laliberté, M.-E. Boulanger, A. Ataei, G. Grissonnanche, D. LeBoeuf, S. Licciardello, S. Wiedmann, S. Ono, H. Raffy, S. Kawasaki, G.-Q. Zheng, N. Doiron-Leyraud, C. Proust, and L. Taillefer, *Physical Review B* **104**, 014515 (2021), 2008.13692.
  - [39] Y. Wang, Z. A. Xu, T. Kakeshita, S. Uchida, S. Ono, Y. Ando, and N. P. Ong, *Physical Review B* **64**, 224519 (2001), [cond-mat/0108242](https://arxiv.org/abs/cond-mat/0108242).
  - [40] Y. Wang, N. P. Ong, Z. A. Xu, T. Kakeshita, S. Uchida, D. A. Bonn, R. Liang, and W. N. Hardy, *Physical Review Letters* **88**, 257003 (2002), [cond-mat/0205299](https://arxiv.org/abs/cond-mat/0205299).
  - [41] Y. Wang, S. Ono, Y. Onose, G. Gu, Y. Ando, Y. Tokura, S. Uchida, and N. P. Ong, *Science* **299**, 86 (2003).
  - [42] P. Dai, M. Yethiraj, H. A. Mook, T. B. Lindemer, and F. Dogan, *Phys. Rev. Lett.* **77**, 5425 (1996).
  - [43] H. F. Fong, B. Keimer, D. L. Milius, and I. A. Aksay, *Phys. Rev. Lett.* **78**, 713 (1997).
  - [44] H. He, Y. Sidis, P. Bourges, G. D. Gu, A. Ivanov, N. Koshizuka, B. Liang, C. T. Lin, L. P. Regnault, E. Schoenherr, and B. Keimer, *Phys. Rev. Lett.* **86**, 1610 (2001).
  - [45] Y. Gallais, A. Sacuto, P. Bourges, Y. Sidis, A. Forget, and D. Colson, *Phys. Rev. Lett.* **88**, 177401 (2002).
  - [46] L. Zhang and Z.-Y. Weng, *Phys. Rev. B* **90**, 165120 (2014).
  - [47] J.-S. Xu, Z. Zhu, K. Wu, and Z.-Y. Weng, (2023), [arXiv:2306.11096](https://arxiv.org/abs/2306.11096).
  - [48] S.-P. Kou and Z.-Y. Weng, *Phys. Rev. Lett.* **90**, 157003 (2003).
  - [49] Z.-Y. Weng and X.-L. Qi, *Physical Review B* **74**, 144518 (2006), [cond-mat/0603097](https://arxiv.org/abs/cond-mat/0603097).
  - [50] X.-L. Qi and Z.-Y. Weng, *Phys. Rev. B* **76**, 104502 (2007).
  - [51] P. Ye, C.-S. Tian, X.-L. Qi, and Z.-Y. Weng, *Phys. Rev. Lett.* **106**, 147002 (2011), 1007.2507.
  - [52] P. Ye, C.-S. Tian, X.-L. Qi, and Z.-Y. Weng, *Nuclear Physics B* **854**, 815 (2012), 1106.1223.

- [53] J. W. Mei and Z. Y. Weng, *Phys. Rev. B* **81**, 014507 (2010).
- [54] C. P. Poole, R. Prozorov, H. A. Farach, and R. J. Creswick, in *Superconductivity (Third Edition)*, edited by C. P. Poole, R. Prozorov, H. A. Farach, and R. J. Creswick (Elsevier, London, 2014) third edition ed., pp. 355–424.
- [55] M. P. A. Fisher and D. H. Lee, *Phys. Rev. B* **39**, 2756 (1989).
- [56] X. G. Wen and A. Zee, *Int. J. Mod. Phys. B* **04**, 437 (1990).
- [57] Note that the doping density can generally be expressed as  $\delta/2 = p/q$ . In instances where  $p = 1$  the lowest Landau level for  $\tilde{E}_m$  remains degenerate. However, further splitting can occur when  $p \neq 1$ . Despite this, the energy associated with such splitting is significantly smaller than the splitting effects induced by magnetic fields, specifically  $\tilde{A}_0^h$  and  $|B^e|$ . Consequently, these energy differences can be disregarded. As a result, all these modes are considered to reside within the lowest energy sector, denoted by  $m \in \text{LES}$ .
- [58] In the scenario where  $p \neq 1$ , the lowest excited level, denoted by energy  $E_s$  as depicted in Fig. 3(a), undergoes a minor splitting, resulting in each split band carrying a more intricate Chern number. Nevertheless, the cumulative Chern number, represented by  $\sum_{m \in \text{LES}} \mathcal{C}_{m\sigma\nu} = \nu$ , is derived from the summation across all these sub-bands.
- [59] D. Xiao, M.-C. Chang, and Q. Niu, *Reviews of Modern Physics* **82**, 1959 (2010), 0907.2021.
- [60] V. Kalmeyer and R. B. Laughlin, *Physical Review Letters* **59**, 2095 (1987).
- [61] X. G. Wen, *Physical Review B* **41**, 12838 (1990).
- [62] T. Qin, Q. Niu, and J. Shi, *Physical Review Letters* **107**, 236601 (2011), 1108.3879.
- [63] T. Qin, J. Zhou, and J. Shi, *Physical Review B* **86**, 104305 (2012), 1111.1322.
- [64] R. Matsumoto and S. Murakami, *Physical Review B* **84**, 184406 (2011), 1106.1987.
- [65] R. Matsumoto and S. Murakami, *Physical Review Letters* **106**, 197202 (2011), 1103.1221.
- [66] M. Plate, J. D. F. Mottershead, I. S. Elfimov, D. C. Peets, R. Liang, D. A. Bonn, W. N. Hardy, S. Chiuazbalian, M. Falub, M. Shi, L. Patthey, and A. Damascelli, *Phys. Rev. Lett.* **95**, 077001 (2005).
- [67] A. Kaminski, S. Rosenkranz, H. M. Fretwell, Z. Z. Li, H. Raffy, M. Randeria, M. R. Norman, and J. C. Campuzano, *Phys. Rev. Lett.* **90**, 207003 (2003).
- [68] U. Chatterjee, D. Ai, J. Zhao, S. Rosenkranz, A. Kaminski, H. Raffy, Z. Li, K. Kadowaki, M. Randeria, M. R. Norman, and J. C. Campuzano, *Proc. Natl. Acad. Sci.* **108**, 9346 (2011).
- [69] S.-P. Kou, X.-L. Qi, and Z.-Y. Weng, *Physical Review B* **72**, 165114 (2005), cond-mat/0412146.
- [70] M. Levin and T. Senthil, *Physical Review B* **70**, 220403 (2004), cond-mat/0405702.
- [71] T. Senthil, A. Vishwanath, L. Balents, S. Sachdev, and M. P. A. Fisher, *Science* **303**, 1490 (2004), cond-mat/0311326.
- [72] C. Wang, A. Nahum, M. A. Metlitski, C. Xu, and T. Senthil, *Physical Review X* **7**, 031051 (2017), 1703.02426.
- [73] R. Coldea, S. M. Hayden, G. Aeppli, T. G. Perring, C. D. Frost, T. E. Mason, S.-W. Cheong, and Z. Fisk, *Physical Review Letters* **86**, 5377 (2001), cond-mat/0006384.
- [74] N. S. Headings, S. M. Hayden, R. Coldea, and T. G. Perring, *Physical Review Letters* **105**, 247001 (2010), 1009.2915.
- [75] H. F. Fong, B. Keimer, P. W. Anderson, D. Reznik, F. Doğan, and I. A. Aksay, *Phys. Rev. Lett.* **75**, 316 (1995).
- [76] B. Fauque, Y. Sidis, L. Capogna, A. Ivanov, K. Hradil, C. Ulrich, A. I. Rykov, B. Keimer, and P. Bourges, *Phys. Rev. B* **76**, 214512 (2007).
- [77] L. Capogna, B. Fauque, Y. Sidis, C. Ulrich, P. Bourges, S. Pailhes, A. Ivanov, J. L. Tallon, B. Liang, C. T. Lin, A. I. Rykov, and B. Keimer, *Phys. Rev. B* **75**, 060502(R) (2007).
- [78] H. F. Fong, P. Bourges, Y. Sidis, L. P. Regnault, A. Ivanov, G. D. Gu, N. Koshizuka, and B. Keimer, *Nature* **398**, 588 (1999).
- [79] H. He, P. Bourges, Y. Sidis, C. Ulrich, L. P. Regnault, S. Pailhes, N. S. Berzigiarova, N. N. Kolesnikov, and B. Keimer, *Science* **295**, 1045 (2002).
- [80] P. Dai, H. A. Mook, S. M. Hayden, G. Aeppli, T. G. Perring, R. D. Hunt, and F. Dogan, *Science* **284**, 1344 (1999).
- [81] M. K. Chan, C. J. Dorow, L. Mangin-Thro, Y. Tang, Y. Ge, M. J. Veit, G. Yu, X. Zhao, A. D. Christianson, J. T. Park, Y. Sidis, P. Steffens, D. L. Abernathy, P. Bourges, and M. Greven, *Nature Communications* **7**, 10819 (2016), 1402.4517.
- [82] M. K. Chan, Y. Tang, C. J. Dorow, J. Jeong, L. Mangin-Thro, M. J. Veit, Y. Ge, D. L. Abernathy, Y. Sidis, P. Bourges, and M. Greven, *Physical Review Letters* **117**, 277002 (2016), 1610.01097.
- [83] S. Pailhès, Y. Sidis, P. Bourges, V. Hinkov, A. Ivanov, C. Ulrich, L. P. Regnault, and B. Keimer, *Physical Review Letters* **93**, 167001 (2004), cond-mat/0403609.
- [84] S. M. Hayden, H. A. Mook, P. Dai, T. G. Perring, and F. Dogan, *Nature* **429**, 531 (2004).
- [85] J. M. Tranquada, H. Woo, T. G. Perring, H. Goka, G. D. Gu, G. Xu, M. Fujita, and K. Yamada, *Nature* **429**, 534 (2004), cond-mat/0401621.
- [86] K. Sato, K. Ikeuchi, R. Kajimoto, S. Wakimoto, M. Arai, and M. Fujita, *J. Phys. Soc. Jpn.* **89**, 114703 (2020), <https://doi.org/10.7566/JPSJ.89.114703>.
- [87] J.-X. Zhang, C. Chen, J.-H. Zhang, and Z.-Y. Weng, (2023), arXiv:2307.05671.
- [88] W. Q. Chen and Z. Y. Weng, *Phys. Rev. B* **71**, 134516 (2005).
- [89] J.-X. Zhang and Z.-Y. Weng, (2022), arXiv:2208.10519.
- [90] N. E. Hussey, M. Abdel-Jawad, A. Carrington, A. P. Mackenzie, and L. Balicas, *Nature* **425**, 814 (2003).
- [91] B. Vignolle, A. Carrington, R. A. Cooper, M. M. J. French, A. P. Mackenzie, C. Jaudet, D. Vignolles, C. Proust, and N. E. Hussey, *Nature* **455**, 952 (2008).
- [92] E. I. Rashba, L. E. Zhukov, and A. L. Efros, *Physical Review B* **55**, 5306 (1997), cond-mat/9603037.

## Supplementary Materials for: “Thermal Hall and Neutral Spinon in a Doped Mott Insulator”

In the following supplementary materials, we provide more analytical results to support the conclusions presented in the main text. In Appendix A, a comprehensive derivation for the effective Lagrangian of chiral spinons, characterized by both chirality  $\nu = \pm$  and spin  $\sigma = \uparrow, \downarrow$ , is presented. Appendix B provides a rigorous derivation elucidating the relationship Eq. (11) between the superconductor critical temperature  $T_c$  and the lowest excitation energy  $E_s$  associated with chiral spinons. Lastly, Appendix C is dedicated to the derivation of the transverse transport coefficient.

### Appendix A: Effective Lagrangian of Chiral Spinons

Upon the condensation of holons and following the decomposition  $h_I = \sqrt{n_I^h} e^{i\theta_I}$  up to the second order of  $\delta n_I^h = n_I^h - \bar{n}_I^h$  and  $\theta_I$ , one can integrate out the amplitude fluctuation  $\delta n_I^h$ . To account for the interaction between holons, we introduce an additional term,  $u(n_I^h)^2/2$ . With this, the Lagrangian Eq. (1) can be recast as:

$$L_h = \sum_I \frac{1}{2u} [\partial_\tau \theta_I - A_0^s(I) - eA_0^e(I)]^2 - i\bar{n}^h [A_0^s(I) + A_0^e(I)] + t_h \bar{n}^h \left[ \Delta_\alpha \theta_I - A_\alpha^s(I) - \frac{e}{\hbar} A_\alpha^e(I) + 2\pi m_\alpha(I) \right]^2 \quad (\text{AS1})$$

in which the Villian expansion

$$e^{\gamma \cos \Delta_\alpha \theta_I} \simeq \sum_{\{m_\alpha \in \mathbb{Z}\}} e^{-\frac{\gamma}{2} [\Delta_\alpha \theta_I + 2\pi m_\alpha(I)]^2} \quad (\text{AS2})$$

is applied. Proceeding further, integrating out the  $A_0^s$  and  $A_\alpha^s$  fields yields:

$$L_h + L_{CS} = \frac{u}{2\pi^2} [B^h(i) - \pi \bar{n}^h]^2 + \frac{1}{4t_h \bar{n}^h \pi^2} (\mathbf{E}^h(i) \cdot \mathbf{z})_\alpha^2 - \frac{ie}{\pi} \sum_i e^{\mu\nu\lambda} A_\mu^e \partial_\nu A_\lambda^h - \frac{i}{\pi} A_\lambda^h \epsilon^{\lambda\nu\mu} 2\pi \partial_\nu m_\mu \quad (\text{AS3})$$

In conjunction with the  $L_s$  term in Eq. (2), integrating out the  $A_0^h$  produces a logarithmic attraction:

$$-\frac{\pi n_h t_h}{2} \sum_{i \neq j} q_i \ln \left( \frac{|r_i - r_j|}{a} \right) q_j \quad (\text{AS4})$$

where  $q_i \equiv \sum_\sigma n_{i,\sigma}^b + 2J_0^{2\pi} + \frac{\Phi^e}{\pi}$  represents the local total chirality. It's noteworthy that the logarithmic interaction can result in a divergent energy over long distances. Therefore, the condition for finite energy leads to the subsequent neutral condition:

$$\sum_\sigma n_{i,\sigma}^b - 2J_0^{2\pi} + \frac{\Phi^e}{\pi} = 0, \quad (\text{AS5})$$

which aligns with Eq. (9) in the main text. Subsequently, let us introduce the vortex operator  $\Phi_i^\dagger \equiv e^{i \sum_{l \neq i} n_l^h \theta_l}$ . This operator satisfies the commutation relations:  $[\Phi_i^\dagger, J_0^{2\pi}(j)] = \Phi_i^\dagger \delta_{i,j}$ ,  $[\Phi_i, \Phi_j^\dagger] = 0$  and  $\Phi_i^\dagger \Phi_i = 1$ . Consequently, we can construct the four lowest energy vortex excitations,  $b_{i\sigma\nu}^\dagger$ , with winding numbers  $\pm$ , as follows:

$$b_{i\uparrow+}^\dagger \equiv b_{i\uparrow+}^\dagger, \quad b_{i\uparrow-}^\dagger \equiv b_{i\uparrow+}^\dagger \Phi_i, \quad (\text{AS6})$$

$$b_{i\downarrow-}^\dagger \equiv b_{i\downarrow+}^\dagger, \quad b_{i\downarrow+}^\dagger \equiv b_{i\downarrow+}^\dagger \Phi_i^\dagger. \quad (\text{AS7})$$

These excitations adhere to the bosonic commutation relations. Hence, in conjunction with Eq. (AS3), the Lagrangian characterizing the physical behavior of these low-lying excitations is denoted by  $\tilde{L} = \tilde{L}_b + \tilde{L}_{MCS}$ , which is expressed as:

$$\tilde{L}_s = \sum_{i\sigma\nu} b_{i\sigma\nu}^\dagger \left[ \partial_\tau - i\nu A_0^h(i) + \lambda_b + \frac{1}{2} g\mu_B B^e \sigma \right] b_{i\sigma\nu} - J_s \sum_{i\alpha\sigma\nu} \left[ b_{i\sigma\nu}^\dagger b_{i+\alpha,\bar{\sigma}\bar{\nu}}^\dagger e^{i\nu A_\alpha^h(i)} + \text{h.c.} \right] \quad (\text{AS8})$$

$$\tilde{L}_{MCS} = \sum_i \frac{u}{2\pi^2} [B^h(i) - \pi \bar{n}^h]^2 + \frac{1}{4t_h \bar{n}^h \pi^2} (\mathbf{E}^h(i) \cdot \mathbf{z})_\alpha^2 - \frac{ie}{\pi} \sum_i e^{\mu\nu\lambda} A_\mu^h \partial_\nu A_\lambda^e. \quad (\text{AS9})$$

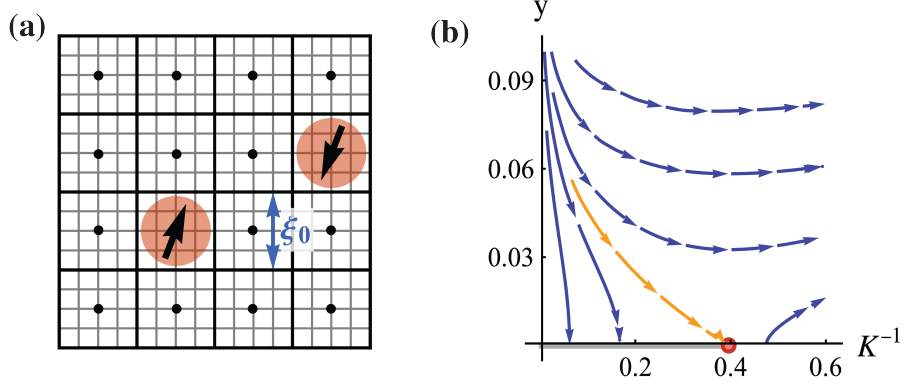


FIG. BS1. (a) The von Neumann lattice with the lattice constants  $\xi_0$  is depicted with black lines. And the original lattice is illustrated with gray lines and has lattice constants  $a$ . The  $b$ -spinon wave packets, labeled by red disks, are positioned at the center  $\mathbf{R}_m$  of the von Neumann lattice, marked by black points. (b) Illustration of the RG flow corresponding to Eq. (BS12) and Eq. (BS13). Orange arrows indicate the separatrix, while the red point marks the fixed point  $(K^*)^{-1} = \pi/8$  and  $y^* = 0$ .

### Appendix B: Determination of $T_c$

Utilizing the saddle point approximation for  $\tilde{L}_h$ , we have:

$$B^h(i) \rightarrow \bar{B}^h = \pi \bar{n}^h, \quad \mathbf{E}^h(i) \rightarrow \bar{\mathbf{E}}^h = 0. \quad (\text{BS1})$$

Under this approximation,  $b$ -spinons encounter a uniform gauge field imparting a  $\delta\pi$  flux per plaquette. Drawing parallels with the standard diagonalization approach found in the Hofstadter system, the Lagrangian Eq. (AS8) can be reformulated as:

$$\tilde{L}_s = \sum_{i\sigma\nu} b_{i\sigma\nu}^\dagger [\partial_\tau - i\nu A_0^h(i)] b_{i\sigma\nu} + \sum_{m\sigma\nu} E_m \gamma_{m\sigma\nu}^\dagger \gamma_{m\sigma\nu} \quad (\text{BS2})$$

with the  $b$ -spinons spectrum:

$$E_m^b = \sqrt{\lambda_b^2 - (\xi_m^b)^2} \quad (\text{BS3})$$

via introducing the following Bogoliubov transformation:

$$b_{i\sigma\nu} = \sum_m \omega_{m\sigma\nu}(\mathbf{r}_i) \left( u_m \gamma_{m\sigma\nu} - v_m \gamma_{m\bar{\sigma}\bar{\nu}}^\dagger \right), \quad (\text{BS4})$$

where the coherent factors are given by

$$\begin{aligned} u_m &= \sqrt{\frac{1}{2} \left( 1 + \frac{\lambda_b}{E_m^b} \right)} \\ v_m &= \text{sgn}(\xi_m^b) \sqrt{\frac{1}{2} \left( -1 + \frac{\lambda_b}{E_m^b} \right)}. \end{aligned} \quad (\text{BS5})$$

Here,  $\xi_m^b$  as well as  $w_m(\mathbf{r}_i) \equiv w_{m\sigma\nu=+}(\mathbf{r}_i) = w_{m\bar{\sigma}\bar{\nu}}^*(\mathbf{r}_i)$  in Eq. (BS4) are the eigenfunctions and eigenvalues of the following equation:

$$\xi_m^b \omega_m(\mathbf{r}_i) = -\frac{J\Delta^s}{2} \sum_{j=\text{NN}(i)} e^{iA_{ij}^h} \omega_m(\mathbf{r}_j). \quad (\text{BS6})$$

The derived  $b$ -spinon dispersion  $E_m^b$  in Eq. (BS3) is depicted in Fig. 3(a), showcasing dispersionless, ‘‘Landau-level-like’’ discrete energy levels[88, 89] with a gap  $E_s$  (indicated by the red arrow). Our subsequent discussions focus primarily on the lowest Landau level (LLL) where  $E_m = E_s$ . Based on prior research[53, 92? ], within the LLL, the

$w_m$ 's are termed as *local modes* (LM). These have an intrinsic size on the scale of the ‘‘cyclotron length’’, given by  $a_c = 1/\sqrt{\pi\delta}$ . For simplicity, we consider the lattice constant to be  $a = 1$ .

These spinon wave packets, represented by magnetic Wannier wave function  $w_m(\mathbf{r})$ , have an amplitude defined as:

$$O_m(\mathbf{r}_i) \equiv |w_m(\mathbf{r}_i)|^2 \simeq \frac{a^2}{2\pi a_c^2} \exp\left[-\frac{|\mathbf{r}_i - \mathbf{R}_m|^2}{2a_c^2}\right]. \quad (\text{BS7})$$

This peaks at the centers of a von Neumann lattice, with a lattice constant  $\xi_0 = \sqrt{2\pi}a_c$  and the lattice site  $\mathbf{R}_m$ , illustrated in Fig. BS1(a).

Combined with Eq. (BS2) and Eq. (AS9), the saddle point effective Lagrangian becomes:

$$\tilde{L}_{\text{eff}} = \frac{1}{4t_h \bar{n} \hbar \pi^2} (\nabla A_0^h)^2 - iA_0^h \sum_i \sum_{\nu\sigma} \nu n_{i\sigma\nu}^b + E_s \sum_{m \in \text{LL}} \sum_{\sigma\nu} n_{m\sigma\nu}^b, \quad (\text{BS8})$$

where the term  $b_{i\sigma\nu}^\dagger \partial_\tau b_{i\sigma\nu}$  is disregarded under the assumption of a temperature high enough to preclude quantum fluctuations. Further, from Eq. (BS4), we obtain:

$$\sum_{\sigma\nu} \nu n_{i\sigma\nu}^b = \sum_{m \in \text{LL}} O_m(\mathbf{r}_i) \sum_{\sigma\nu} \nu n_{m\sigma\nu}. \quad (\text{BS9})$$

After integrating out  $A_0^h$ , the effective action is described as:

$$S_{\text{eff}} \simeq - \int_0^\beta d\tau \frac{\pi \bar{n} t_h}{2} \sum_{m \neq n} q(\mathbf{R}_m) \ln\left(\frac{|\mathbf{R}_m - \mathbf{R}_n|}{\xi_0}\right) q(\mathbf{R}_n) + \int_0^\beta d\tau E_s \sum_m |q(\mathbf{R}_m)|^2 \quad (\text{BS10})$$

$$= -\frac{\pi}{4} \frac{\rho_s}{k_B T} \sum_{m \neq n} q(\mathbf{R}_m) \ln\left(\frac{|\mathbf{R}_m - \mathbf{R}_n|}{\xi_0}\right) q(\mathbf{R}_n) + \frac{E_s}{k_B T} \sum_m |q(\mathbf{R}_m)|^2, \quad (\text{BS11})$$

where  $t_h = \frac{\hbar^2}{2m_h}$ , the spin stiffness is denoted by  $\rho_s \equiv \bar{n}_h/m_h$ . In this context, Eq. (BS11) represents a two-dimensional neutral Coulomb plasma with unit charge  $q = \pm 1$  situated on the von Neumann lattice. Following this, we can employ a standard approach to address the conventional KT transition. We introduce the reduced stiffness as  $K = \rho_s/k_B T$  and define the effective fugacity of each vortex as  $y \equiv e^{-E_s/k_B T}$ .

The differential renormalization group (RG) equations are then expressed as:

$$\frac{dK^{-1}}{dl} = g^2 \pi^3 y^2 + O(y^4), \quad (\text{BS12})$$

$$\frac{dy}{dl} = \left(2 - \frac{\pi}{4} K\right) y + O(y^3), \quad (\text{BS13})$$

where  $g = 4$  accounts for the degeneracy at each site  $\mathbf{R}_m$  on the von Neumann lattice, arising from time reversal and bipartite lattice symmetries. An observation is that these RG equations remain valid even if we substitute  $(K, y)$  with  $(K4, gy)$  in the conventional KT transition's RG equations. This substitution is attributed to the unit vorticity of each spinon vortex being  $\pi$  instead of  $2\pi$  of a conventional vortex, and  $y$  is replaced by  $gy$  because of the  $g$  degeneracy for each site  $\mathbf{R}_m$  on the von Neumann lattice.

The RG flow is illustrated in Fig. BS1(b), which displays a separatrix, indicated by orange arrows, traversing the critical point  $(K^*)^{-1} = \pi/8$  and  $y^* = 0$ . Points located above this separatrix tend toward larger values of both  $K^{-1}$  and  $y$ , signifying a transition to the phase with unbound vortices corresponding to the SC disordered phase. Conversely, points below this separatrix are towards to the line  $y = 0$ . This indicates a prohibition on free vortex excitation at low temperatures and corresponds to the chiral spinon confinement in the SC phase. The separatrix flow intrinsically determines the SC critical temperature  $T_c$ , which can be found by solving:

$$K_c^{-1} - \pi/8 = -\pi^2 y_c. \quad (\text{BS14})$$

Given the relationship  $k_B T_c/\rho_s \ll \pi/8$ , we deduce:

$$\frac{E_s}{k_B T_c} \simeq 3.22, \quad (\text{BS15})$$

which is consistent with Eq. (11) in the main text. Moreover, by recognizing that  $E_g = 2E_s$ , we can derive Eq. (29).

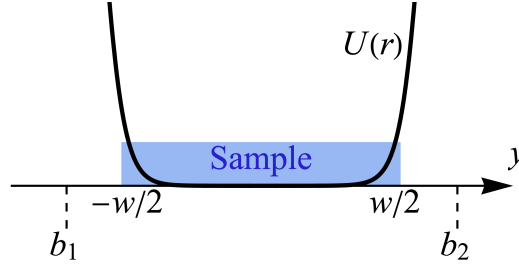


FIG. CS2. Depiction of a sample characterized by a width  $w$ , utilized in the determination of the edge current. The potential  $U(\mathbf{r})$  acts as a confining mechanism within the sample.

### Appendix C: Derivation of Semi-Classical transport coefficient

The velocity of a wave packet is characterized by the semiclassical equation of motion, incorporating the topological Berry phase term:

$$\mathbf{v} \equiv \dot{\mathbf{r}} = \frac{1}{\hbar} \frac{\partial \epsilon_n(\mathbf{k})}{\partial \mathbf{k}} - \dot{\mathbf{k}} \times \boldsymbol{\Omega}_n(\mathbf{k}) \quad (\text{CS1})$$

where  $n$  denotes the band index,  $\epsilon_n(\mathbf{k})$  represents the energy dispersion of the  $n$ -th band, and the Berry curvature in momentum space is given by  $\boldsymbol{\Omega}_n(\mathbf{k}) = i \nabla_{\mathbf{k}} \times \langle u_n(\mathbf{k}) | \nabla_{\mathbf{k}} | u_n(\mathbf{k}) \rangle$ . It's worth noting that  $\hbar \dot{\mathbf{k}} = -\nabla U(\mathbf{r})$ , where  $U(\mathbf{r})$  is a confining potential present only near the boundary of the sample. This potential ensures that the wave packet of particles remains within the sample, and its gradient applies a force on the particles.

Let us consider a sample delineated by a boundary, with a coordinate system as depicted in Fig. CS2. Here,  $w$  signifies the system's width in the  $y$ -direction, and  $b_1, b_2$  represent the  $y$ -axis coordinates of the boundary where  $U(b_1) = U(b_2) = \infty$ . From the second term of Eq. (CS1), close to the sample's boundary, there emerges an edge current directed along the  $x$ -axis. The current density is obtained by summing up the local velocity  $\mathbf{v}_x(y)$  and dividing it by the width:

$$J_x = \frac{1}{w} \int_{b_1}^{b_2} \frac{1}{V} \mathbf{v}_x(y) dy \quad (\text{CS2})$$

$$= \frac{1}{w} \int_{b_1}^{b_2} \frac{1}{\hbar V} \sum_{\mathbf{k}, m} n(\epsilon_m(\mathbf{k}) + U(y); T(y)) [\partial_y U(y)] \boldsymbol{\Omega}_m(\mathbf{k}) dy \quad (\text{CS3})$$

$$\simeq -\frac{1}{w} \sum_{\mathbf{k}, m} \int_{\epsilon_m(\mathbf{k})}^{\infty} \frac{1}{\hbar V} n\left(\epsilon; T\left(-\frac{w}{2}\right)\right) \boldsymbol{\Omega}_m(\mathbf{k}) d\epsilon + \frac{1}{w} \sum_{\mathbf{k}, m} \int_{\epsilon_m(\mathbf{k})}^{\infty} \frac{1}{\hbar V} n\left(\epsilon; T\left(\frac{w}{2}\right)\right) \boldsymbol{\Omega}_m(\mathbf{k}) d\epsilon \quad (\text{CS4})$$

$$= \frac{1}{w} \int \partial_y \left[ \frac{1}{\hbar V} \sum_{\mathbf{k}, m} \int_{\epsilon_m(\mathbf{k})}^{\infty} n(\epsilon; T(y)) \boldsymbol{\Omega}_m(\mathbf{k}) d\epsilon \right] dy \quad (\text{CS5})$$

where the current here means the current of the particle number,  $V$  is the area of the sample and  $n(\epsilon; T) = [e^{(\epsilon-\mu)/k_B T} - 1]^{-1}$  is the bosonic distribution. Analogously, the energy current derived from the edge current density is expressed as:

$$(J_E)_x^{\nabla T} = \frac{1}{w} \int \partial_y \left[ \frac{1}{\hbar V} \sum_{\mathbf{k}, m} \int_{\epsilon_n(\mathbf{k})}^{\infty} \epsilon \times n(\epsilon; T(y)) \boldsymbol{\Omega}_m(\mathbf{k}) d\epsilon \right] dy. \quad (\text{CS6})$$

Given a temperature gradient along the  $y$ -direction, the gradient in particle distribution is formulated as:

$$\partial_y n(\epsilon; T(y)) = (\epsilon - \mu) \frac{\partial n}{\partial \epsilon} T \frac{\partial \beta}{\partial y}, \quad (\text{CS7})$$



which leads to the edge current density as well as the energy current:

$$(J)_x^{\nabla T} = \frac{1}{w} \int \left[ \frac{1}{\hbar V} \sum_{\mathbf{k}, m} \int_{\epsilon_m(\mathbf{k})}^{\infty} (\epsilon - \mu) \frac{\partial n}{\partial \epsilon} T \frac{\partial \beta}{\partial y} \Omega_m(\mathbf{k}) d\epsilon \right] dy \quad (\text{CS8})$$

$$(J_E)_x^{\nabla T} = \frac{1}{w} \int \left[ \frac{1}{\hbar V} \sum_{\mathbf{k}, m} \int_{\epsilon_m(\mathbf{k})}^{\infty} \epsilon (\epsilon - \mu) \frac{\partial n}{\partial \epsilon} T \frac{\partial \beta}{\partial y} \Omega_m(\mathbf{k}) d\epsilon \right] dy. \quad (\text{CS9})$$

Similarly, the chemical potential gradient along the  $y$ -direction can give the particle distribution gradient as follows:

$$\partial_y n(\epsilon(y); T) = -\frac{\partial n(\epsilon; T)}{\partial \epsilon} \frac{\partial \mu}{\partial y}, \quad (\text{CS10})$$

which results in the edge current density and the energy current:

$$(J)_x^{\nabla \mu} = -\frac{1}{w} \int \left[ \frac{1}{\hbar V} \sum_{\mathbf{k}, m} \int_{\epsilon_m(\mathbf{k})}^{\infty} \frac{\partial n(\epsilon; T)}{\partial \epsilon} \frac{\partial \mu}{\partial y} \Omega_n(\mathbf{k}) d\epsilon \right] dy \quad (\text{CS11})$$

$$(J_E)_x^{\nabla \mu} = -\frac{1}{w} \int dy \left[ \frac{1}{\hbar V} \sum_{\mathbf{k}, m} \int_{\epsilon_m(\mathbf{k})}^{\infty} \epsilon \frac{\partial n(\epsilon; T)}{\partial \epsilon} \frac{\partial \mu}{\partial y} \Omega_n(\mathbf{k}) d\epsilon \right] dy \quad (\text{CS12})$$

Now we define a heat current as  $J_Q \equiv J_E - \mu J$  and write down the linear response of the current  $J_x$  and heat current  $(J_E)_x$  by combining Eq. (CS8), Eq. (CS9), Eq. (CS11) and Eq. (CS12):

$$\begin{bmatrix} \mathbf{J}_x^\nu \\ (\mathbf{J}_Q)_x \end{bmatrix} = \mathbf{L}^{\text{xy}} \begin{bmatrix} -\nabla_y \mu \\ T \nabla_y \frac{1}{T} \end{bmatrix}. \quad (\text{CS13})$$

Here,  $\mathbf{L}^{\text{xy}, \nu}$  signifies a  $2 \times 2$  matrix that represents the transverse transport coefficients. The parameter  $\nu = \pm$  distinguishes between the different chiralities of spinon. The matrix elements are given by

$$L_{ij}^{xy} = -\frac{1}{\hbar V \beta q} \sum_m \sum_{\mathbf{k}} c_q [n(\epsilon_m(\mathbf{k}); T)] \Omega_m(\mathbf{k}) \quad (\text{CS14})$$

where  $i, j = 1, 2$  and

$$c_q[x] \equiv \int_0^x \left( \log \frac{1+t}{t} \right)^q dt, \quad (\text{CS15})$$

which is consistent with Eq. (20) in the main text.